AGU Advances

RESEARCH ARTICLE
10.1029/2022AV000751

Peer Review The peer review history for this article is available as a PDF in the Supporting Information.

Key Points:

- We use constitutive models including transient deformation to infer the full-spectrum mechanical behavior of the Greenland upper mantle
- Contribution of transient deformation is most significant over centennial to millennial timescales relating to historical ice mass change
- Transient effects may explain conflicting mantle viscosity and lithosphere thickness estimates from geodetic and geological observations

Supporting Information:

Supporting Information may be found in the online version of this article.

Correspondence to:

G. J. G. Paxman,
guy.j.paxman@durham.ac.uk

Citation:

Paxman, G. J. G., Lau, H. C. P., Austermann, J., Holtzman, B. K., & Havlin, C. (2023). Inference of the timescale-dependent apparent viscosity structure in the upper mantle beneath Greenland. *AGU Advances*, *4*, e2022AV000751. https://doi.org/10.1029/2022AV000751

Received 7 JUN 2022
Accepted 4 FEB 2023

Author Contributions:

Conceptualization: Guy J. G. Paxman, Harriet C. P. Lau, Jacqueline Austermann, Benjamin K. Holtzman, C. Havlin
Data curation: Guy J. G. Paxman, C. Havlin
Formal analysis: Guy J. G. Paxman, Harriet C. P. Lau
Methodology: Guy J. G. Paxman, Harriet C. P. Lau, Jacqueline Austermann, Benjamin K. Holtzman

Inference of the Timescale-Dependent Apparent Viscosity Structure in the Upper Mantle Beneath Greenland

Guy J. G. Paxman[1,2], Harriet C. P. Lau[3], Jacqueline Austermann[1], Benjamin K. Holtzman[1], and C. Havlin[4]

[1]Lamont-Doherty Earth Observatory, Columbia University, Palisades, NY, USA, [2]Department of Geography, Durham University, Durham, UK, [3]Department of Earth, Environmental and Planetary Sciences, Brown University, Providence, RI, USA, [4]School of Information Sciences, University of Illinois Urbana-Champaign, Champaign, IL, USA

Abstract Contemporary crustal uplift and relative sea level (RSL) change in Greenland is caused by the response of the solid Earth to ongoing and historical ice mass change. Glacial isostatic adjustment (GIA) models, which seek to match patterns of land surface displacement and RSL change, typically employ a linear Maxwell viscoelastic model for the Earth's mantle. In Greenland, however, upper mantle viscosities inferred from ice load changes and other geophysical phenomena occurring over a range of timescales vary by up to two orders of magnitude. Here, we use full-spectrum rheological models to examine the influence of transient deformation within the Greenland upper mantle, which may account for these differing viscosity estimates. We use observations of shear wave velocity combined with constitutive rheological models to self-consistently calculate mechanical properties including the apparent upper mantle viscosity and lithosphere thickness across a broad spectrum of frequencies. We find that the contribution of transient behavior is most significant over loading timescales of 10^2–10^3 years, which corresponds to the timeframe of ice mass loss over recent centuries. Predicted apparent lithosphere thicknesses are also in good agreement with inferences made across seismic, GIA, and flexural timescales. Our results indicate that full-spectrum constitutive models that more fully capture broadband mantle relaxation provide a means of reconciling seemingly contradictory estimates of Greenland's upper mantle viscosity and lithosphere thickness made from observations spanning a range of timescales.

Plain Language Summary Glaciated regions such as Greenland experience fluctuations in ice mass on timescales ranging from years to hundreds of thousands of years. Because the Earth is deformable, its surface subsides and rebounds in response to the growth and decay of ice. Studies that focus on the ice-induced deformation of the Earth beneath Greenland over long timescales typically consider a constant viscosity, which governs the rate at which deformation occurs. However, the way the Earth deforms is complex, and includes transient processes that occur over shorter timescales. In this study, we use equations that link the temperature and composition of the Greenland mantle to its mechanical properties at different timescales to estimate the magnitude of these transient effects. We find that the contribution of transient deformation is greatest in response to load changes over hundreds to thousands of years, which may account for seemingly contradictory estimates of viscosity made from observations of deformation over these timescales. We conclude that it is important to consider transient mantle behavior in Greenland to predict crustal deformation and relative sea level change more accurately across a broad range of timescales.

1. Introduction

Glacial isostatic adjustment (GIA) is defined as the response of the solid Earth and global gravity field to changes in the distribution of ice and water on Earth's surface (Whitehouse et al., 2019). The surface manifestations of GIA include vertical land motion, relative sea level (RSL) change, and changes in coastlines, all of which can be measured in regions proximal and distal to past and present ice sheets. In Greenland, contemporary crustal motion and RSL change are attributed to the ongoing adjustment of the solid Earth to changes in ice mass since the Last Glacial Maximum (LGM; ca. 21 ka) (Khan et al., 2008; Simpson et al., 2011). Around much of the Greenland coastline, RSL is currently falling due to a combination of (a) isostatic uplift of the land surface induced by historical and contemporary ice sheet retreat and mass loss (Figures 1a and 1b) (Khan et al., 2016), and (b) a reduction in the height of the geoid caused by the weakening gravitational attraction of the diminishing Greenland Ice Sheet (Spada et al., 2012). Robust predictions of future RSL change caused by past, present and future ice mass loss are vital for assessing the impact on coastlines and shallow-water environments (Nicholls &

Software: Benjamin K. Holtzman, C. Havlin
Writing – original draft: Guy J. G. Paxman
Writing – review & editing: Harriet C. P. Lau, Jacqueline Austermann, Benjamin K. Holtzman, C. Havlin

Cazenave, 2010). This is especially pertinent in Greenland, where communities are almost exclusively located along the coast and rely on nearshore waterways for transportation, fishing and hunting, commercial activity, and tourism (Lyck & Taagholt, 1987).

The development of more accurate projections of the magnitude and pattern of future RSL change around Greenland is reliant on GIA models, which combine an understanding of changes in ice mass and the rheological properties of the solid Earth. To confidently forecast future sea level change, GIA models seek to accurately hindcast past and contemporary change. In particular, they aim to account for (a) patterns of RSL change preserved in the geological record (e.g., isolation basin sediments, marine fossil assemblages, raised shorelines, and archeological data) (Long et al., 2011), and (b) present-day rates of vertical land motion measured by global navigation satellite system (GNSS) networks (Dietrich et al., 2005; Khan et al., 2016). This can help constrain the ice load history and mantle rheology, both of which govern the pattern and rate of solid Earth deformation and sea level change.

Historically, most GIA studies have simulated solid Earth deformation using a linear Maxwell viscoelastic model, with an instantaneous elastic response superimposed on a longer-term viscous relaxation. The mechanical properties that define the Maxwell model are the unrelaxed elastic (shear) modulus, which governs the amplitude of the elastic response, and the steady-state viscosity, which governs the rate of the viscous deformation. Many GIA models assume a radially symmetric Earth divided into a finite number of layers (e.g., lithosphere, upper mantle, and lower mantle, where the latter two are divided by the 670 km seismic discontinuity), each characterized by a single steady-state viscosity (Peltier et al., 2015). This is typically accompanied by a radial density and elastic moduli profile which may vary at much finer length scales (e.g., Dziewonski & Anderson, 1981). However, the thermodynamic state of the Earth is strongly heterogeneous, which causes rheological properties to not only vary radially, but also laterally within the mantle. This has resulted in the development of more sophisticated 3D viscoelastic models, where viscosity varies as a function of latitude, longitude, and depth (e.g., Milne et al., 2018; van der Wal et al., 2015).

In addition, recent studies have suggested that mechanical behavior more complex than the linear Maxwell model may be required to account for certain aspects of Earth deformation observed across a range of timescales (Caron et al., 2017; Lau et al., 2020; Lau & Holtzman, 2019). More complex linear viscoelastic models include a transient (anelastic) regime of deformation, which results in the apparent viscosity being dependent on the frequency of the particular (un)loading process (Ivins et al., 2020). Additional complexity can also arise from non-linearity, where the strain rate and/or magnitude of stress may cause changes in the viscosity through dislocation creep-related processes (Blank et al., 2021; Kang et al., 2022; van der Wal et al., 2015). The mantle viscosity inferred from geological and/or geodetic observations may therefore be dependent on: (a) the thermodynamic state of the mantle, which is laterally variable, (b) the depth range within the mantle over which deformation is induced by the (un)loading, (c) the frequency (timescale) at which the (un)loading occurs, and (d) the level of stress in the mantle.

GIA models often tune mantle viscosity structure to fit the constraints provided by RSL data spanning the time interval since the LGM. In Greenland, the optimal upper mantle viscosity inferred from GIA modeling of post-LGM RSL data is $\sim 5 \times 10^{20}$ Pa s, with a best-fitting elastic lithosphere thickness of 120 km (Figures 1c and 1d) (Lecavalier et al., 2014; Simpson et al., 2009). However, explicit consideration of the ongoing response of the solid Earth to more recent ice mass loss since the Little Ice Age (LIA; Figure 1b), which concluded at ca. 1850–1900 CE (Kjeldsen et al., 2015; Mankoff et al., 2021), is necessary to account for misfits between observed GNSS-derived uplift rates and GIA models that only consider post-LGM deglaciation (Adhikari et al., 2021). Moreover, these data-model misfits can be explained only for scenarios where the mantle viscosity is reduced by approximately one order of magnitude to $6–11 \times 10^{19}$ Pa s, and as low as 3×10^{19} Pa s in the upper mantle if a stratified mantle model is assumed (Figure 1d) (Adhikari et al., 2021).

Adhikari et al. (2021) suggest that this discrepancy, whereby upper mantle viscosities inferred from GNSS data pertaining to ice loss and GIA over multi-decadal/centennial timescales are lower than viscosities inferred from RSL data pertaining to multi-millennial timescales, is indicative of the need to consider models of transient deformation, which capture mantle relaxation across a range of timescales. The incorporation of transient behavior can act to lower the apparent viscosity on shorter timescales (Lau & Holtzman, 2019), and may therefore provide an explanation for the more rapid uplift rates associated with post-LIA mass changes (Adhikari et al., 2021).

The definition of the lithosphere also depends on the timescale of observation (Figure 1c). In studies focusing on geological timescales associated with GIA and flexural isostasy, the lithosphere is mechanically defined as

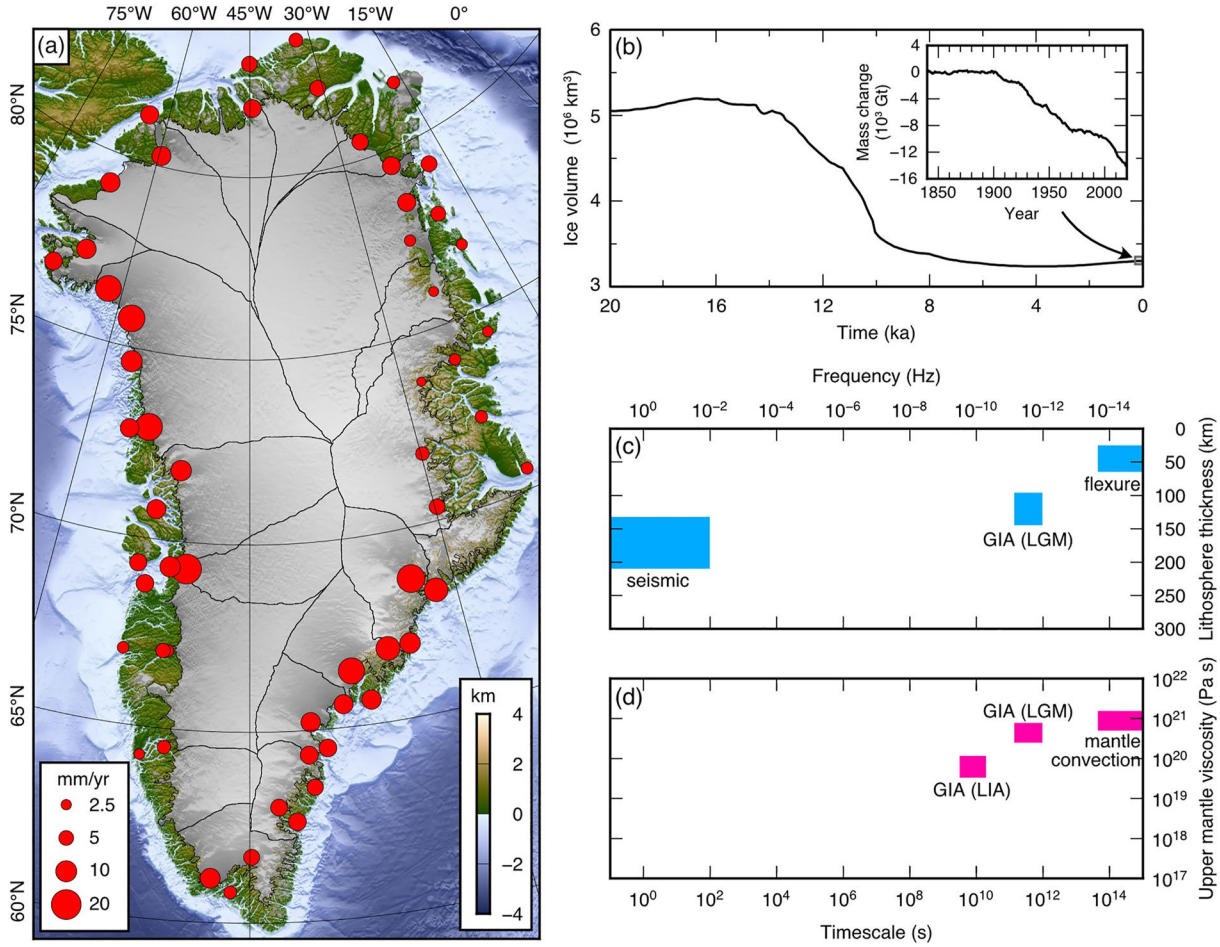

Figure 1. Ice sheet change and glacial isostatic adjustment in Greenland. (a) Study area map. The Greenland Ice Sheet is shaded in gray; land surface topography and seafloor bathymetry are displayed according to the color scale (relative to mean sea level) (Morlighem et al., 2017). Black lines demarcate major ice sheet drainage basins (Zwally et al., 2012). Red circles mark the positions of global navigation satellite system stations, with their size proportional to the average crustal uplift rate (Adhikari et al., 2021). (b) Model prediction of Greenland ice volume since the Last Glacial Maximum (LGM; ca. 21 ka) (Lecavalier et al., 2014). Inset: reconstruction of cumulative ice mass change since 1840 CE, showing mass loss since the end of the Little Ice Age (LIA) (Mankoff et al., 2021). Note that for ice 1 Gt ≈ 1 km^3. (c) Compilation of apparent lithosphere thickness estimates in Greenland from observations at differing timescales. Observations from glacial isostatic adjustment (GIA) and flexural isostasy (Lecavalier et al., 2014; Steffen et al., 2018) infer a shallower lithosphere than those using seismic shear wave velocities (Priestley & McKenzie, 2013). (d) Compilation of Greenland upper mantle viscosity estimates (Adhikari et al., 2021; Lecavalier et al., 2014; Steinberger et al., 2015). All estimates were inferred using a linear Maxwell model with a single steady-state viscosity. In panels (c) and (d), the lithosphere thickness and upper mantle viscosity values are spatial averages for Greenland, and the ranges in magnitude reflect stated uncertainties or the standard deviations of spatially variable fields. The frequency bands spanned by the non-seismic inferences were approximated based on the timescales swept by each process.

the layer that deforms elastically with no viscous component (Lecavalier et al., 2014; Steffen et al., 2018). At seismic timescales, seismic waves capture a snapshot of the present thermodynamic state, which can be mapped onto that expected for a thermally-defined lithosphere (Priestley & McKenzie, 2013) in which a conductive, high viscosity boundary layer forms atop a convecting interior (Jaupart & Mareschal, 2007; Sleep, 2005). While higher-frequency body wave measurements reveal that the transition from the lithosphere to asthenosphere is often sharper than expected for a classical thermal lithosphere, requiring additional variations in thermodynamic state (Fischer et al., 2010), the seismically observed lithosphere at both surface and body wave frequencies is deeper than that for GIA and flexural isostasy (Figure 1c).

The aim of this study is to quantify the role of transient mantle deformation beneath Greenland and determine whether the incorporation of transient processes can reconcile contrasting estimates of mantle viscosity and lithosphere thickness derived from data sets that relate to different timescales of deformation. We begin by using the inferred mechanical properties of the Greenland upper mantle at the seismic timescale to perform a 3D inversion of the mantle thermodynamic state. From this, we employ two commonly used phenomenological

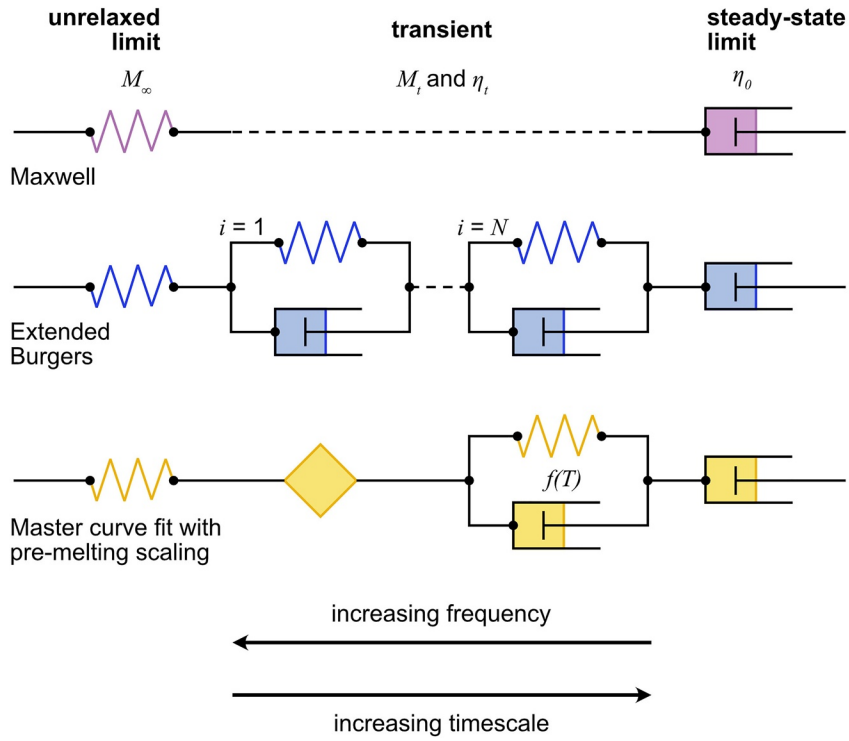

Figure 2. Schematic diagram of commonly used phenomenological models of viscoelastic deformation, illustrated in terms of combinations of mechanical springs and dashpots. The symbols M and η represent the modulus of the spring and viscosity of the Newtonian dashpot fluid, respectively. M_∞ refers to the unrelaxed (infinite-frequency) elastic modulus, η_0 to the steady-state (zero-frequency) viscosity, and M_t and η_t to the transient regime. Note that the diamond represents an infinite sum of Kelvin-Voigt units (spring and dashpot in parallel).

(laboratory-derived) models of mantle rheology to determine the contribution of transient deformation across a broad range of frequencies (timescales). Finally, we compare our results to observations and assess the importance of incorporating transient deformation mechanisms in future models of mantle rheology in Greenland.

2. Full-Spectrum Models of Viscoelastic Deformation

The rheology of the solid Earth is challenging to understand because geodetic and geological observations contain signals from multiple deformation processes that operate over a broad range of spatial and temporal scales. Moreover, the Earth's response to these processes varies substantially across a broad spectrum of rheological behavior. At very short timescales encompassed by global seismological observations (seconds to minutes), Earth deformation is dominated by elasticity, with limited attenuation of seismic waves as they propagate. The elastic response is instantaneous, reversible, non-dissipative, and can be described as “anharmonic” since it occurs at the infinite frequency limit with no frequency dependence. Moving toward very long timescales associated with major glacial cycles and planetary-scale deep Earth processes (hundreds of thousands to millions of years), there is a transition to steady-state viscous deformation. Toward this zero-frequency limit, the viscous response is time-dependent, irreversible, and completely dissipative.

The widely used linear Maxwell viscoelastic model combines the instantaneous elastic and steady-state viscous responses (Figure 2). However, observations from rock mechanics (e.g., Jackson & Faul, 2010), post-seismic relaxation (e.g., Pollitz, 2003), lake rebound (e.g., Bills et al., 2007), and GIA (Lau et al., 2021; Simon et al., 2022) indicate that, in addition to these two end members, there is also a transient regime of deformation where strain is time-dependent yet reversible. This suggests that more complex rheological models that incorporate transient (anelastic) deformation may be required to unify load-induced Earth deformation processes that operate across the full-spectrum of timescales from seconds to millions of years.

Transient dissipation has been characterized by results from laboratory experiments, where mantle-representative materials (e.g., olivine or polycrystalline analogs such as borneol) are subjected to a range of pressure and

temperature conditions (Gribb & Cooper, 1998; Jackson & Faul, 2010; McCarthy & Takei, 2011; Yamauchi & Takei, 2016). The result is a semi-empirical ("experimental") constitutive law between stress and strain rate, which may then be scaled to mantle conditions. This constitutive relationship can be expressed as a phenomenological model of anelastic deformation analogous to the linear Maxwell model (Figure 2), from which we can derive frequency-dependent viscoelastic parameters such as the complex modulus and the complex viscosity (Lau & Holtzman, 2019).

However, the transient regime is more complex and less well understood than the elastic and viscous responses, and as a result a number of different anelastic constitutive models have been proposed (Gribb & Cooper, 1998; Jackson & Faul, 2010; Yamauchi & Takei, 2016). In our analysis we used the open-source software library known as the Very Broadband Rheology calculator (VBRc; Havlin et al., 2021) to self-consistently predict the elastic, anelastic, and viscous mechanical properties of the Greenland upper mantle based on inferences of the mantle thermodynamic state made using observations at the seismic timescale. We performed this analysis for two widely used, yet distinct, anelastic constitutive models to allow for the lack of complete understanding in the rock mechanics community. We provide a brief overview of these constitutive models here; for full details of the equations and constants for these models we refer the reader to Havlin et al. (2021).

2.1. Extended Burgers Model With Pseudoperiod Scaling

The extended Burgers model is a phenomenological model of linear viscoelasticity, where multiple relaxation mechanisms may be superimposed (Jackson & Faul, 2010). Conceptually, the extended Burgers model includes a finite number of Kelvin-Voigt elements (a spring and dashpot in parallel), which represent the transient regime (Figure 2) between the instantaneous elastic and steady-state viscous limits that characterize the linear Maxwell model (a spring and dashpot in series).

2.2. Master Curve Fit With Pre-Melting Scaling Using Near-Solidus Parameterization

The master curve fit model uses an empirically derived fit for the relaxation function. It includes an additional parameterization at temperatures approaching the solidus to allow for a marked reduction in viscosity and increase in attenuation near the melting point, which arises due to the change in physical state of grain boundaries at these temperatures, prior to the formation of the melt phase (Yamauchi & Takei, 2016). Conceptually, the transient regime of the master curve fit model can be envisaged as an infinite sum of Kelvin-Voigt elements with an additional Kelvin-Voigt element whose modulus and viscosity are functions of temperature (Figure 2).

These two constitutive models are known to make different predictions on account of the means of scaling from laboratory to mantle conditions and intrinsic sensitivities to certain parameters (e.g., the grain size exponent differs notably between the two models (Havlin et al., 2021; Ivins et al., 2022)). We primarily present the predictions of the master curve fit model (Yamauchi & Takei, 2016) in our results, since this model incorporates a scaling term at high temperatures that can account for experimental and real-world observations such as the rapid increase in attenuation and decrease in shear wave velocity near the solidus. This has led to this parameterization being adopted in a variety of geodynamic studies (e.g., Austermann et al., 2021; Ball et al., 2019; Richards et al., 2020). Versions of the extended Burgers model, which typically predicts higher steady-state viscosities, have also been frequently used in rock physics, post-seismic relaxation, and GIA studies (Caron et al., 2017; Faul & Jackson, 2005; Ivins et al., 2022). We therefore compare the predictions of the master curve fit and extended Burgers models at relevant points in our analysis.

3. Methods

We used a three-stage workflow to predict the upper mantle mechanical properties across the entire frequency spectrum for Greenland. First, we extracted estimates of the mechanical properties of the upper mantle in the seismic band from a recent tomography model. Second, we used a linearized 3D Bayesian inversion and the seismic properties to constrain the thermodynamic state of the upper mantle using the constitutive equations for both rheological models described in Section 2. Third, we used the same constitutive equations to self-consistently predict the complex moduli across the full frequency spectrum, encapsulating the elastic, anelastic, and viscous regimes. In the second and third stages the VBRc was employed to map between thermodynamic state variables

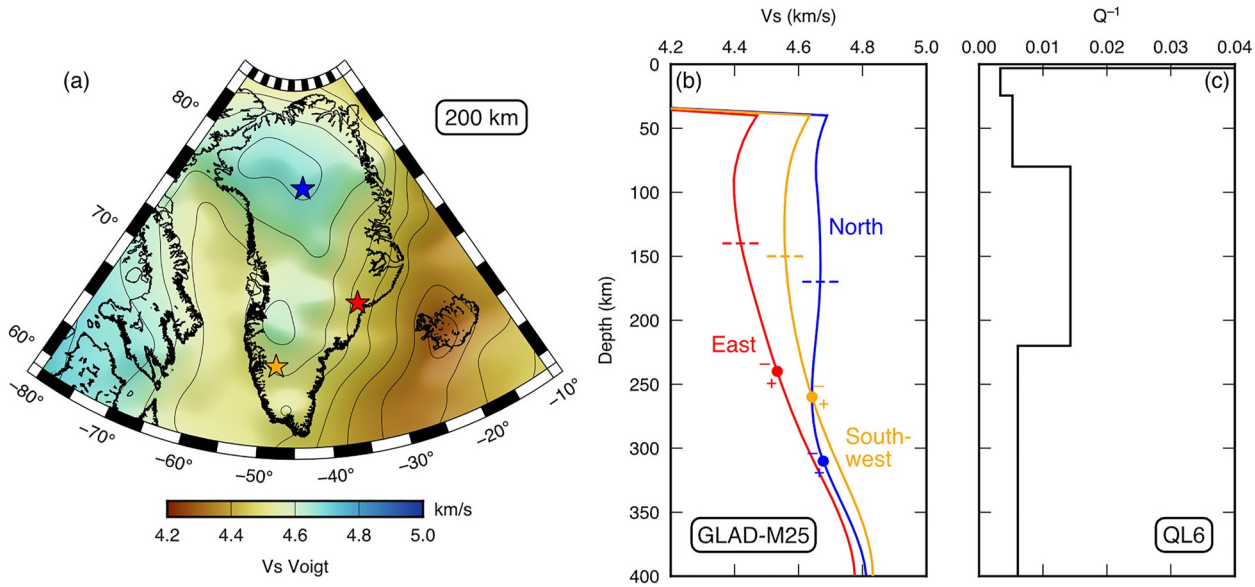

Figure 3. (a) Voigt-averaged shear wave velocities (*Vs*) at 200 km depth from the GLAD-M25 global adjoint tomography model (Lei et al., 2020). The model resolution is 0.5°, but for efficiency we downsampled the model onto a 2° mesh for our calculations. (b) Depth profiles of *Vs* at the three selected localities in north, east, and southwest Greenland marked by the colored stars in panel (a). Circles show the depth at which the down-profile velocity anomaly switches from negative to positive. The dashed horizontal lines show the inferred lithosphere-asthenosphere boundary depth (mid-point of the negative velocity anomaly) for the seismic model. (c) QL6 1D global attenuation (Q^{-1}) model (Durek & Ekström, 1996), which was used within the construction of the GLAD-M25 shear wave velocity model.

and mechanical properties at the relevant frequency bands. For full self-consistency, the constitutive model used in each inversion in stage two was always the same as that used in the corresponding calculation in stage three. A similar approach was applied by Lau et al. (2021) for locations across Antarctica, although in this case only 1D profiles of subsurface structure were considered.

3.1. Mechanical Properties From Seismic Tomography

Inferences of the mechanical properties of the upper mantle are commonly made within the seismic band (i.e., close to the elastic limit). Specifically, we are interested in the isotropic shear wave velocity (*Vs*), the intrinsic attenuation (Q^{-1}), and the lithosphere thickness. For *Vs*, we computed the Voigt averaged shear wave velocity from the anisotropic global adjoint tomography model GLAD-M25 (Lei et al., 2020) (Figures 3a and 3b) referenced at 1 Hz, which is defined as

$$V s_{\text{Voigt}} = \sqrt{\frac{V_{\text{SH}}{}^2 + 2V_{\text{SV}}{}^2}{3}}, \tag{1}$$

where V_{SH} and V_{SV} are the model horizontal and vertical shear wave velocities, respectively.

GLAD-M25 was constructed using the QL6 1D global attenuation model (Durek & Ekström, 1996). Therefore, since QL6 is embedded in *Vs*, we used QL6 as our Q^{-1} model (at its 1 Hz reference frequency). As a result, unlike *Vs*, Q^{-1} varies only in the radial direction (Figure 3c). The attenuation is defined as

$$Q^{-1} = \frac{J_2}{J_1}, \tag{2}$$

where J_1 is the compliance and J_2 is the loss compliance. While using a 1D Q^{-1} model in our 3D inversion may introduce artifacts in the thermodynamic state solution, this is the most consistent approach given that the GLAD-M25 *Vs* model assumes a 1D Q^{-1} profile, and still provides an additional constraint on the thermodynamic state compared to relying on *Vs* alone. Ideally, both a 3D *Vs* and Q^{-1} model would be used, but global attenuation models have not yet achieved the same level of consistency as *Vs* models (Bao et al., 2016).

GLAD-M25 is a global model constructed with a horizontal resolution of 0.5° and a vertical resolution of 10 km. For computational efficiency, we downsampled the *Vs* model to 2° horizontal resolution and defined the limits of

the Greenland model domain as the region between 80° and 10°W and 59° and 84°N and from 40 km (the assumed base of the crust) to 400 km depth (Figure 3). We also used the GLAD-M25 *Vs* model to estimate the depth to the lithosphere-asthenosphere boundary (LAB) across the region (Figure S1 in Supporting Information S1). At each grid point, we determined a *Vs* anomaly profile (i.e., the deviation from the depth-averaged velocity); these profiles typically show a transition from negative velocity anomalies at shallow depths to positive anomalies at deeper levels (Figure 3b). We set the LAB depth to be the mid-point between the minimum and maximum depths at which the velocity anomaly is negative (Figure 3b). We note that this is just one of multiple possible definitions for the LAB depth (Eaton et al., 2009; Fischer et al., 2010). However, this approximate estimate is useful for placing an upper bound on the LAB depth at short timescales and for examining spatial patterns.

3.2. Inference of the Thermodynamic State: 3D Bayesian Inversion

The next step in our methodology was to use a Bayesian inversion to constrain the 3D thermodynamic state of the mantle that most likely explains the seismic 3D *Vs* and 1D Q^{-1} models. The Bayesian inference framework allows us to use a prior assumption of the likely thermodynamic state and incorporate the uncertainties inherent in this prior assumption as well as those present in the input seismic model (*Vs* and Q^{-1}). It also provides a means of examining the trade-off between, and sensitivity of the complex moduli to, the thermodynamic state variables.

In this context, the thermodynamic state of the mantle refers to the combination of state variables at any location, including temperature, composition, grain size, melt fraction, differential stress, and water content. Here, we aim to constrain three state variables—temperature, melt fraction, and grain size—which are allowed to vary laterally and radially in the inversion. The pressure and temperature dependence of mantle density was determined using the equation of state in Grose and Afonso (2013; see Section 4.1 therein). Knowledge of both pressure and density allows for self-consistent conversion to depth which is in turn used to connect these state variables to nodes within the GLAD-M25 tomography model.

All other state variables are held constant in space; we assumed a bulk composition of olivine rock with 90% forsterite, a typical dissolved water content of 100 ppm (Bell & Rossman, 1992), and a mean differential stress of 0.5 MPa, a reasonable average given that viscoelastic loading calculations suggest that over a deglaciation cycle the upper mantle stress driven by GIA varies between 0 and 2 MPa (Lau et al., 2021). Although composition, water content, and differential stress would also be expected to vary spatially, the direct effect of water content on the anelastic regime is currently not well constrained and therefore not implemented in the VBRc. Differential stress can affect attenuation through dislocation damping, but these effects are not yet well constrained from experiments, so the VBRc only considers linear (stress and strain amplitude-independent) anelasticity (see Havlin et al. (2021) for further discussion). The effect of composition on peridotite anelasticity is the subject of several studies (e.g., Sundberg & Cooper, 2010), but the scaling to mantle conditions is not well constrained, so not incorporated into the VBRc (Havlin et al., 2021). Varying these parameters is therefore beyond the scope of this study.

We first established a prior model that represents pre-existing knowledge of, or hypotheses for, the possible probabilities of the free state variables (temperature, melt fraction, and grain size). For the prior model we assumed that temperature is the single most important parameter for governing the seismic properties and viscoelastic moduli, assuming the pressure is known (Cammarano et al., 2003; Stixrude & Lithgow-Bertelloni, 2005). We therefore created an initial ("first guess") temperature distribution on the simplified premise that all the spatial variation in *Vs* and Q^{-1} is linked to temperature. To achieve this, we used the VBRc to predict values of *Vs* and Q^{-1} across our domain for temperatures ranging from 1100°C to 1800°C (a realistic and sufficiently wide range). The temperature distribution that best fitted the seismic model was in turn assigned as the mean of the prior model, with an assumed Gaussian distribution with a standard deviation of ±100°C. The mechanical properties from the chosen constitutive model were evaluated at the appropriate frequency of 1 Hz.

For melt fraction, we assumed a spatially uniform Gaussian prior distribution with a mean value of 0.01 and a standard deviation of ±0.0025. This distribution assumes that upper mantle melt fractions are low (McKenzie, 2000; Takei, 2017), while allowing for scenarios ranging from negligible melt to a small but appreciable melt fraction, as might be expected for a model domain including a craton and a mid-ocean ridge (Havlin et al., 2021). For grain size, we based our prior on mantle xenoliths recovered from Palaeogene basaltic lavas and dykes in east and west Greenland, which show average grain sizes on the order of 1 mm diameter, and a range of 0.1–10 mm (Bernstein et al., 1998, 2006). We therefore assumed a log-normal prior distribution for grain size, with a mean diameter of

1 mm and a standard deviation in log-space of ±0.2 log units (i.e., $10^{0 \pm 0.2}$ mm). In addition, the modal forsterite content of the olivine grains is 92%–94%, which agrees well with our assumed mantle olivine composition.

Quantification of the uncertainty in *Vs* and Q^{-1} is challenging for seismic tomographic models (Rawlinson et al., 2014). We assumed a spatially uniform uncertainty of ±0.1 km/s for *Vs*, which reflects the maximum difference between the GLAD-M25 model and the NAT2021 regional North Atlantic tomographic model (Celli et al., 2021) in the domain of interest, and a conservative ±50 for Q (note that $Q^{-1} = 1/Q$) since we use a 1D global model. Our inversion adopts a Bayesian methodology in which the seismic model inferences and their uncertainties are combined with the prior probability distribution for the state variables to produce a posterior distribution of the state variables. Since we are inverting for a three-dimensional distribution of the three state variables, we used a smoothing factor with a length scale of 200 km to produce a realistically smooth posterior distribution. It is important to note that the assumed prior standard deviations are relatively tight and there are more degrees of freedom than we can constrain using the seismic model inferences (*Vs* and Q^{-1}) alone. The use of a Bayesian approach ensures that these limitations are openly considered, and allows us to determine, given these assumptions, the expected variations in the three state variables that have the strongest influence on transient deformation. The posterior distributions (maximum likelihood solution and standard deviation) should therefore be interpreted with the prior distributions in mind.

We used an iterative algorithm to compute the posterior distribution, which incorporates the uncertainties associated with the seismic inferences and the prior distribution (Lau et al., 2016; Tarantola & Valette, 1982). The maximum likelihood solution is given by the final model iterate

$$\hat{\mathbf{X}}_{k+1} = \hat{\mathbf{X}}_k + \left(\mathbf{F}_k^T \mathbf{V}_\xi^{-1} \mathbf{F}_k + \mathbf{V}_{PR}^{-1}\right)^{-1} \times \left\{\mathbf{F}_k^T \mathbf{V}_\xi^{-1} \left(\mathbf{y} - f\left(\hat{\mathbf{X}}_k\right)\right) - \mathbf{V}_{PR}^{-1}\left(\hat{\mathbf{X}}_k - \mathbf{X}_{PR}\right)\right\}, \tag{3}$$

where $\hat{\mathbf{X}}_0$ is the starting model and $\mathbf{F}_0$ is the matrix of Fréchet kernels (i.e., partial derivatives) associated with the starting model (these matrices change for each k-th iterate). $\mathbf{V}_\xi$ is the covariance matrix of the observational data uncertainties, $\mathbf{X}_{PR}$ is the prior model, $\mathbf{V}_{PR}$ is the covariance matrix of the prior model uncertainties, $\mathbf{y}$ is the observational data vector, and $f\left(\hat{\mathbf{X}}_k\right)$ is a forward prediction of the data vector based on the k-th model iterate. The covariance matrix of the posterior distribution may be approximated as (Lau et al., 2016; Tarantola & Valette, 1982)

$$\mathbf{V}_{PO} \approx \left[\mathbf{F}^T \mathbf{V}_\xi^{-1} \mathbf{F} + \mathbf{V}_{PR}^{-1}\right]^{-1}, \tag{4}$$

where $\mathbf{F}$ is the matrix of Fréchet kernels computed using the final model iterate. We used a finite difference approach to compute the partial derivatives, using the VBRc to perform the forward calculations required to achieve this. The diagonal elements of the $\mathbf{V}_{PO}$ matrix contain the variances (squares of the standard deviations) of the maximum likelihood solution, and the off-diagonals contain the covariances, which provide a measure of the relationship between each state variable at any given location and all other state variables at all other locations in the model domain. Separate inversions were performed for both the extended Burgers and master curve fit constitutive models (Sections 2.1 and 2.2).

3.3. Calculation of Apparent Viscosity and LAB Depth Across the Frequency Spectrum

The thermodynamic states determined via our Bayesian inversion were then used as inputs in the VBRc to calculate the full-spectrum mechanical behavior of the Greenland mantle spanning all timescales for each constitutive model. We used the maximum likelihood combination of temperature, melt fraction, and grain size, along with the other fixed thermodynamic state variables (Section 3.2). In the VBRc, the elastic calculations were performed using anharmonic state variables (i.e., pressure and temperature) to calculate the elastic moduli such as the unrelaxed shear modulus (M_∞) (Havlin et al., 2021). The anelastic calculations employed the constitutive equations of the two phenomenological models described in Section 2 to compute the complex moduli. The viscous calculations used the corresponding "flow laws" to determine the steady-state viscosity (η_0) (Jackson & Faul, 2010; Yamauchi & Takei, 2016). These equations are summarized in recent publications (Havlin et al., 2021; Lau et al., 2021) and in the VBRc documentation (https://vbr-calc.github.io/vbr/).

For any thermodynamic state and phenomenological model, the VBRc computes the complex modulus ($M^*(\omega)$), which is the frequency-dependent coefficient that links stress and strain. Lau and Holtzman (2019) explored a

related parameter referred to as the complex viscosity ($\eta^*(\omega)$), which is the frequency-dependent coefficient that links stress and strain rate. The complex viscosity is defined as (Lau & Holtzman, 2019)

$$\eta^*(\omega) = -\frac{i}{\omega} M^*(\omega). \tag{5}$$

The complex modulus and the complex viscosity can be determined as continuous functions across all frequencies for any arrangement of springs and dashpots, including the linear Maxwell model (Lau et al., 2021). We then computed the apparent viscosity as the magnitude of $\eta^*(\omega)$. It is important to note that the apparent viscosity is not directly analogous to the viscosity of the steady-state dashpot (i.e., the quantity usually reported by studies that use the linear Maxwell model to match observations of RSL change and land uplift), except at the zero-frequency limit, where $\|(\eta^*(\omega))\|$ converges to the steady-state viscosity (η_0).

For each phenomenological model, we calculated an additional frequency-dependent quantity known as the normalized complex viscosity (Lau & Holtzman, 2019)

$$\overline{\eta}^*(\omega) = \frac{\|\eta^*(\omega)\|}{\|\eta^*_{MX}(\omega)\|}, \tag{6}$$

where $\|(\eta^*_{MX}(\omega))\|$ is the apparent viscosity associated with a linear Maxwell model with the same end-member mechanical properties (M_∞ and η_0) as the particular phenomenological model under consideration, that is,

$$\eta^*_{MX}(\omega) = -\frac{i}{\omega}\left(\frac{i\omega\eta_0}{1 + i\omega\frac{\eta_0}{M_\infty}}\right). \tag{7}$$

As a result, the normalized complex viscosity will be equal to 1 at the elastic and viscous limits. Any departure from unity at intermediate frequencies will be the result of the transient creep processes included in the phenomenological model acting as an additional source of dissipation. Therefore, the normalized complex viscosity can be used to identify the frequency interval within which there is a significant contribution from transient deformation for a particular thermodynamic state and phenomenological model. Within these frequency bands, any inference of a Maxwell steady-state viscosity may be contaminated by transient dissipation.

We also examined the frequency dependence of the apparent lithospheric thickness. To do so, we calculated the Maxwell frequency, which is a depth-dependent material property given by the ratio between the unrelaxed shear modulus and the steady-state viscosity (i.e., the reciprocal of the Maxwell time),

$$\omega_{MX}(z) = \frac{M_\infty(z)}{\eta_0(z)}. \tag{8}$$

At a given frequency, the base of the lithosphere can be defined as the depth at which the Maxwell frequency is equal to that frequency,

$$z_{\mathrm{LAB}}(\omega) = z|_{\omega=\omega_{MX}(z)}. \tag{9}$$

In this way, the LAB is defined as the depth above which elastic deformation is dominant, and below which viscous deformation is dominant (Lau et al., 2020). This depth, $z_{\mathrm{LAB}}(\omega)$, therefore marks the depth of the transition from elastic to viscous behavior at any particular frequency (Lau et al., 2021). We used Equation 9 to determine $z_{\mathrm{LAB}}(\omega)$ at each location in the model domain. We note that at high (e.g., seismic body and surface wave propagation) frequencies, this definition of the LAB breaks down because the frequency becomes higher than the Maxwell frequency at all depths and the entire mantle behaves as an elastic half-space (Watts et al., 2013), and thus the notion of an "elastic plate" becomes mechanically irrelevant. We therefore impose a condition that at high frequencies the LAB depth is given by the seismic lithosphere thickness determined using *Vs* tomography (see Section 3.1).

4. Results

To illustrate the spatial variability in the inferred thermodynamic state and mechanical properties of the Greenland mantle, we examine (a) lateral variation at the 200 and 400 km depth slices, which encompass the depth

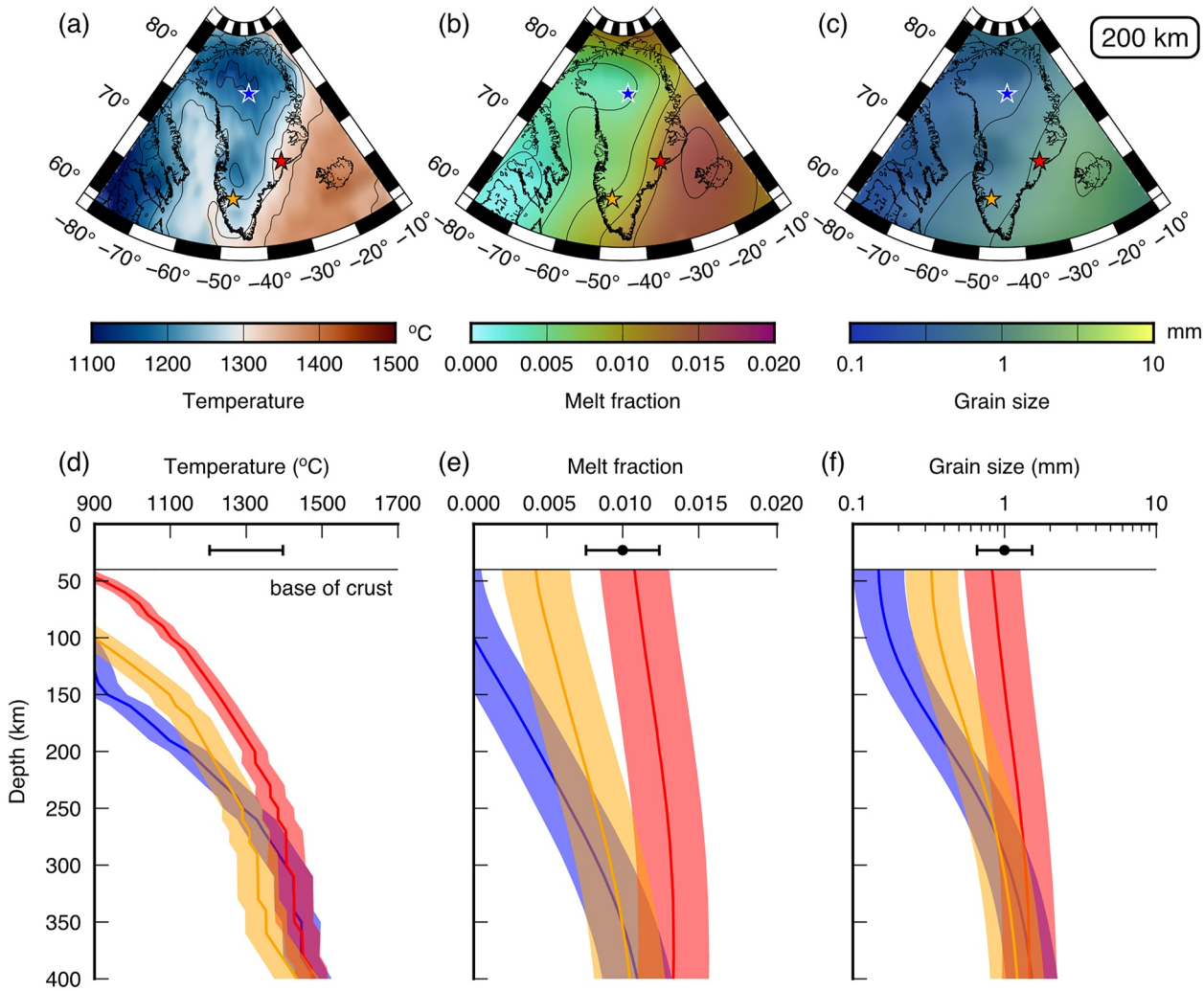

Figure 4. Thermodynamic state of the upper mantle beneath Greenland and surrounding areas derived via Bayesian inversion. Upper row: maps of the maximum likelihood solution for (a) temperature (contour interval = 50°C), (b) melt fraction (contour interval = 0.0025), and (c) grain size (contour interval = 0.25 log units) at 200 km depth. Lower row: vertical profiles of the posterior distributions of (d) temperature, (e) melt fraction, and (f) grain size at the three selected localities in Greenland (see colored stars in panels (a–c)). Solid lines mark the maximum likelihood (mean) solution, and colored bands indicate ± one standard deviation; we assumed that the prior and posterior uncertainties are normally distributed about the mean. The mean (black circle) and standard deviation (black bars) of the prior model are shown for reference; these should be borne in mind when interpreting the posterior distributions. The sharpness in the temperature profiles is inherited from the prior model being produced by assuming all spatial variation in Vs and Q^{-1} is temperature-driven (see Section 3.2); this is also why there is not a single mean value for the temperature prior.

interval of the upper mantle between the base of the lithosphere and the base of the model domain, for which contrasting viscosities have been previously reported, and (b) radial variation at three sites in east, southwest, and north Greenland, which captures the observed range of high- and low-velocity regions.

4.1. Thermodynamic State of the Greenland Upper Mantle

The thermodynamic state inversion produces a plausible maximum likelihood (mean) solution for mantle temperature, melt fraction and grain size. Mantle temperatures are primarily situated within the range 1100°C–1500°C, with steep vertical thermal gradients in the upper ∼250 km of the mantle, and more uniform values of 1300°C–1500°C attained below this depth (Figure 4). The temperature field exhibits lateral variability, with temperatures at 200 km depth exceeding 1400°C beneath east Greenland and Iceland, but less than 1200°C beneath northern Greenland and Canada (Figure 4a). The degree of lateral variability decreases with depth (Figure S2 in Supporting Information S1), reflecting the reduced heterogeneity of seismic velocities at depths of 300–400 km in the mantle (Figure 3b).

Inferred sub-lithospheric melt fractions are <0.01 beneath most of Greenland, with higher values of 0.01–0.015 below east Greenland and ~0.02 beneath Iceland and the Mid-Atlantic Ridge. These values are consistent with the ranges found by a number of previous studies (Evans et al., 1999; Forsyth et al., 1998; Naif et al., 2013). Across most of the region, the mantle grain size is inferred to reside in the range 0.1–1.0 mm, with larger multi-millimeter values occurring beneath east Greenland and Iceland (Figure 4c). The standard deviations of the maximum likelihood thermodynamic state variables primarily reflect the assumed prior uncertainty (Figures 4d–4f). We found that it was necessary to use a relatively tightly defined grain size prior to produce a plausible thermodynamic state (Havlin et al., 2021). If the grain size prior was relaxed (i.e., the standard deviation was increased), we witnessed a trade-off between melt fraction and temperature that resulted in unrealistically high melt fractions below much of Greenland. Given this sensitivity, better constraints on these priors will be valuable for future studies that aim to infer the thermodynamic state of any mantle region (Lau et al., 2021).

4.2. Apparent Mantle Viscosity

Using our inversion results, we calculated the apparent viscosity by taking the magnitude of the complex viscosity, which was determined according to Equation 5. The apparent viscosity (as for all complex moduli) was computed at each point in the 3D model domain. However, for simplicity, and because the lithosphere is effectively treated as a non-viscous layer in GIA models by using arbitrarily high viscosities, we only display the computed apparent viscosity at depths below the seismic LAB.

We find that the apparent viscosity shows a dependence on the frequency (timescale) of the forcing/loading. At frequencies corresponding to timescales of 10–30 years, which aligns with ice mass change during the satellite era, the apparent viscosity at 200 km depth is on the order of 10^{18} Pa s for the master curve fit model (Figure 5a). For frequencies equivalent to 100–200-year timescales, corresponding to the ice mass change and GIA following the LIA, the apparent viscosity increases to values on the order of 10^{19} Pa s (Figure 5b). At timescales of 10–20 thousand years, corresponding to the ice mass change and GIA following the LGM, the mean apparent viscosity increases to values on the order of 10^{20} Pa s (Figure 5c). At very low frequencies (i.e., multi-million-year timescales associated with deep Earth processes like mantle convection), the mean apparent upper mantle viscosity stabilizes at $\sim 6 \times 10^{20}$ Pa s (Figure 5d), which can be thought of as approximating the average steady-state viscosity at the zero-frequency limit (η_0) in this region. Apparent viscosity patterns at 400 km are similar to 200 km, with the exception that lateral variation at lower frequencies is more muted at 400 km than at 200 km (Figure S2 in Supporting Information S1), as is the case for the thermodynamic state.

The degree of lateral and radial variability in the apparent viscosity also increases with the timescale of loading. The apparent viscosity shows minimal depth variation for timescales shorter than 200 years (i.e., compare Figure 5 and Figure S2 in Supporting Information S1), whereas at multi-millennial and longer timescales a 100–200 km-thick low-viscosity layer is present immediately below the lithosphere (Figures 5e–5g). The apparent viscosity of this layer is up to one order of magnitude lower than the underlying mantle. At higher frequencies (shorter timescales), apparent viscosities also exhibit very little lateral variation (Figures 5a and 5b), whereas at lower frequencies (longer timescales) we observe lateral heterogeneities of up to two orders of magnitude (Figures 5c and 5d). For example, at post-LGM and longer timescales the apparent uppermost mantle (200 km) viscosity varies between values on the order of 10^{19} Pa s in Baffin Bay, 10^{20} Pa s in southern and eastern Greenland, and 10^{21} Pa s in northern Greenland (Figures 5c and 5d). This result arises because the complex viscosity is dominated by variations in the steady-state viscosity (η_0) at low frequencies and in the unrelaxed shear modulus (M_∞) at high frequencies (Figure S3 in Supporting Information S1). The shear modulus is not strongly sensitive to temperature, as evidenced by the observation that lateral variations in shear wave velocity are typically less than ±5% (Karato & Karki, 2001), whereas the steady-state viscosity is strongly temperature-dependent (Barnhoorn et al., 2011; Hirth & Kohlstedt, 2003). As a result, the complex viscosity is much more strongly dependent on the thermodynamic state at low frequencies than at high frequencies, which we suggest gives rise to the observed trend in the degree of spatial heterogeneity (Figure 5).

When assessing the impact of the uncertainty in the inferred thermodynamic state on the computed apparent viscosity, we need to consider the covariance between the three state variables, which will affect the range of possible viscosities. We find that there is a trade-off (i.e., negative covariance) between temperature and melt fraction (as one increases the other must decrease to hold the apparent viscosity constant). By contrast, an increase in temperature must be accompanied by an increase in grain size to fix the apparent viscosity (i.e., positive covariance; Figures 6a–6c). In the Greenland upper mantle, when each state variable is varied between $\pm 1\sigma$

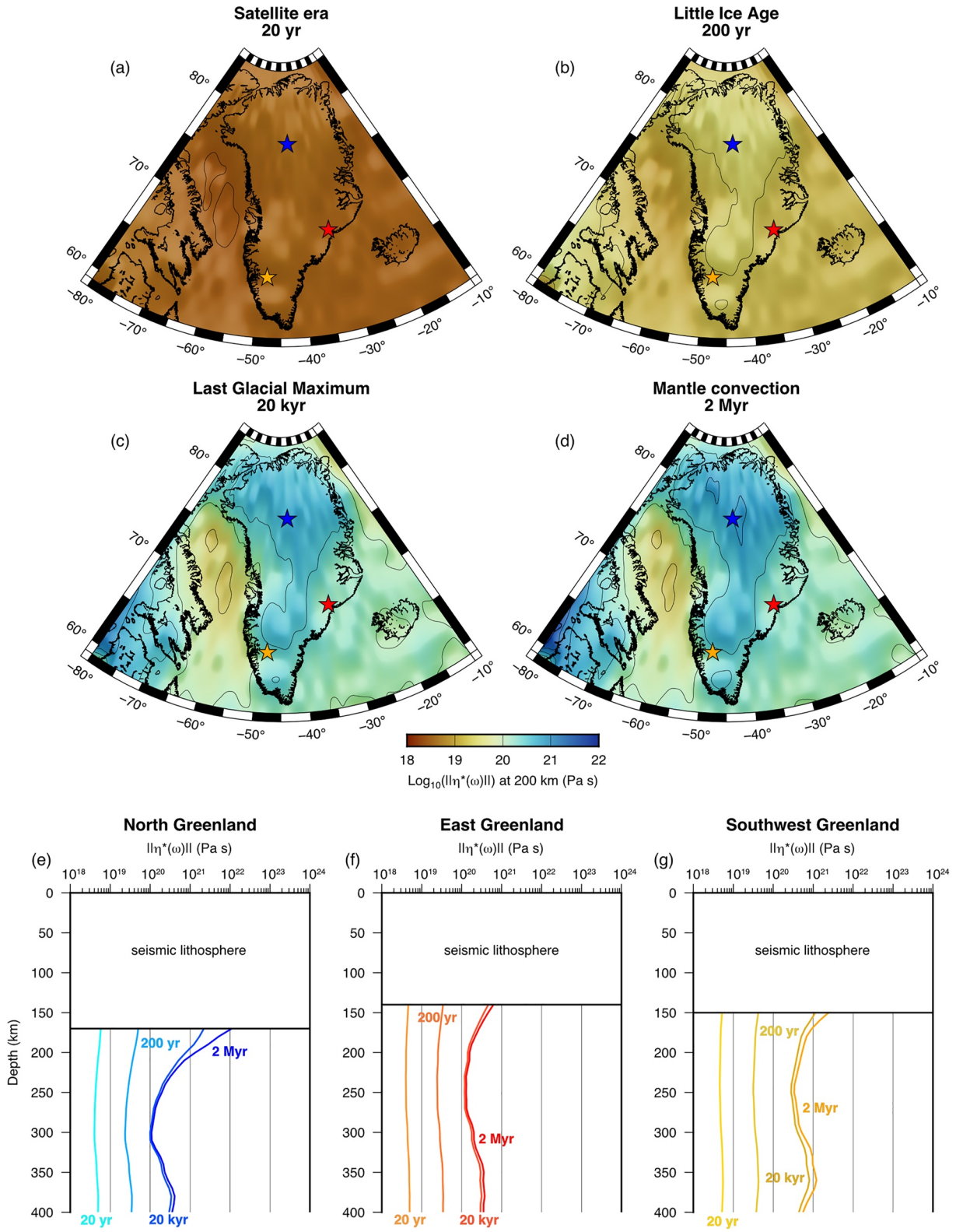

Figure 5. Apparent viscosity at a range of timescales for the master curve fit with pre-melting scaling constitutive model. Maps show the apparent viscosity at 200 km depth at (a) 20 years, (b) 200 years, (c) 20 kyr, and (d) 2 Myr timescales. We assume that the apparent viscosity at very low frequencies (d) approximates the steady-state viscosity. Contour interval is 0.5 log units. Profiles show the apparent viscosity at the four timescales for the sites in (e) northern Greenland, (f) eastern Greenland, and (g) southwestern Greenland (see colored stars for locations). Solid horizontal line marks the seismic lithosphere thickness.

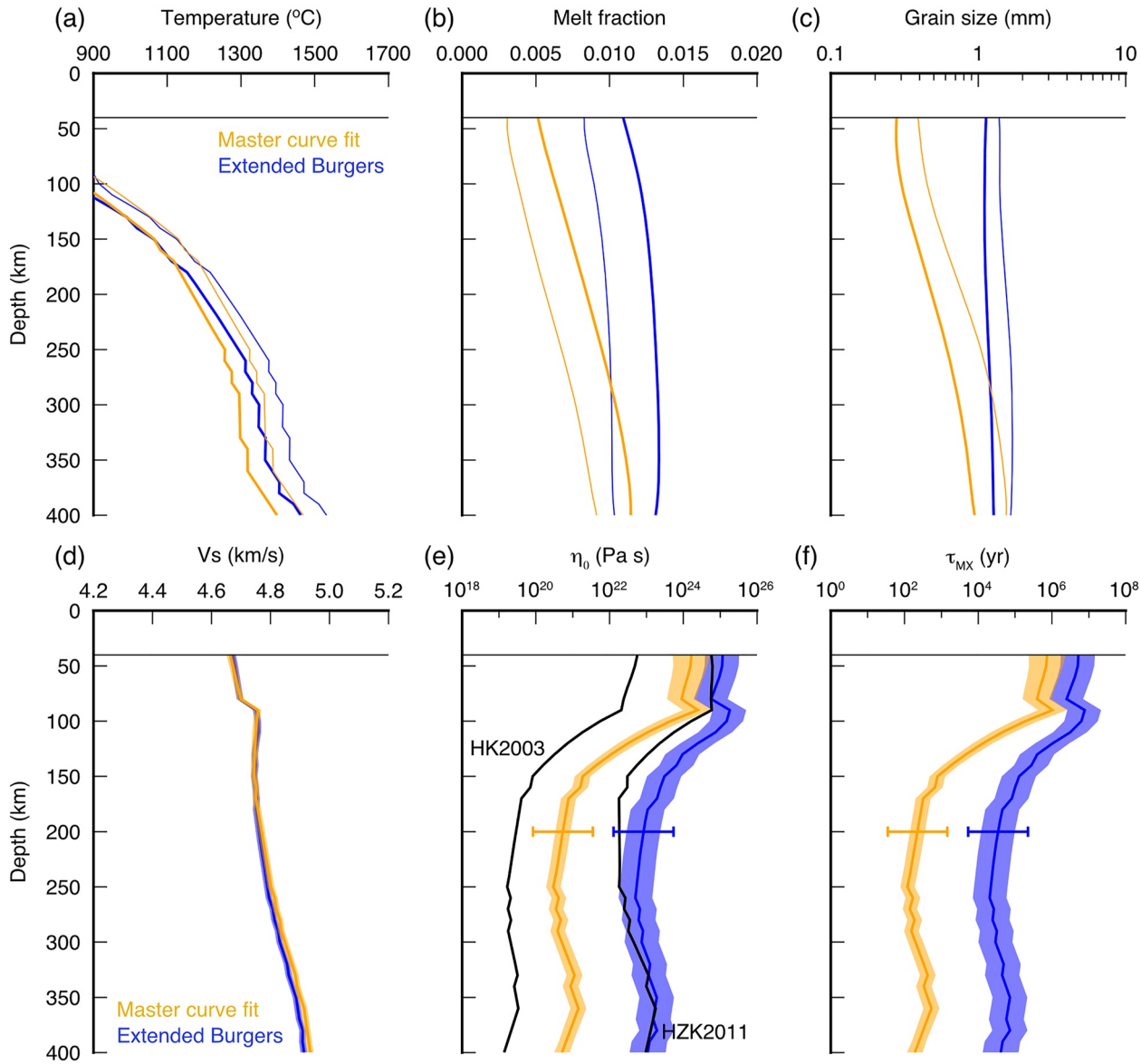

Figure 6. Influence of constitutive models on upper mantle mechanical properties. All profiles are for the site in southwest Greenland. (a) Temperature profiles derived via Bayesian inversion for the master curve fit and extended Burgers constitutive models. For both models, the thick line denotes the lower limit temperature (maximum likelihood -1σ) and the thin line denotes the upper limit temperature (maximum likelihood $+1\sigma$). (b) Corresponding melt fraction profiles calculated using the covariance between temperature and melt fraction. (c) Corresponding grain size profiles calculated using the covariance between temperature and grain size. (d) *Vs* profiles showing the maximum likelihood solution (solid line) and standard deviation (colored bands) after accounting for state variable covariance (a–c). (e) Maximum likelihood and standard deviation of the steady-state viscosity. Black lines show steady-state viscosities for two olivine "flow laws" (Hansen et al., 2011; Hirth & Kohlstedt, 2003) under the same thermodynamic state as used for the master curve fit model. (f) Maximum likelihood and standard deviation of the Maxwell time. In panels (e) and (f), horizontal bars at 200 km show the full range in steady-state viscosity and Maxwell time corresponding to the upper and lower limits of the three state variables (a–c), but the standard deviation is narrower owing to the trade-off between state variables.

and the other two are adjusted according to their respective covariances, the corresponding range in *Vs* is within error (±0.1 km/s; Figure 6d) and the computed apparent viscosity and Maxwell time vary by between 0.5 and 1 orders of magnitude (Figures 6e and 6f). This variation is smaller than the range of values associated with the upper and lower limits of the state variables if covariances are not considered (Figures 6e and 6f); the effect of the uncertainty in the thermodynamic state on the inferred mechanical properties (e.g., *Vs* and viscosity) is reduced owing to the covariance between state variables.

At shorter timescales, the master curve fit and extended Burgers models predict very similar apparent viscosities (compare Figure 5 and Figure S4 in Supporting Information S1), whereas the difference in the average

steady-state viscosity is more than two orders of magnitude (Figure 6e, Figure S4 in Supporting Information S1). This is despite both constitutive models predicting similar maximum likelihood distributions for the thermodynamic state variables in our Bayesian inversion (Figures 6a–6c) and similar mechanical properties at the elastic limit (i.e., *Vs*; Figure 6d). Steady-state viscosities predicted by two alternative olivine "flow laws" using identical thermodynamic states (Hansen et al., 2011; Hirth & Kohlstedt, 2003) differ from each other by approximately three orders of magnitude, although they bracket the master curve fit solution and show similar radial variability (Figure 6e). The steady-state viscosity may also be shifted by other variables held fixed in our analysis (e.g., water content and differential stress; see Section 3.2) that are likely spatially variable in reality. These differences and uncertainties underline the ongoing challenges regarding rock mechanics and the scaling of experimental results to mantle conditions, particularly at geological timescales.

4.3. Apparent Lithosphere Thickness

In the master curve fit model, the apparent LAB depth also shows dependence on the frequency of forcing. Moving toward lower frequencies, z_{LAB} progressively decreases from the imposed condition that it is equal to the seismic lithosphere thickness at high frequencies (Section 3.3, Figure 7a). On post-LIA (100–200 years) timescales, the apparent LAB depth varies from 140 km in southern and eastern Greenland to 230 km in the northwest (Figure 7b). The mean thickness across Greenland is 170 km, which is still close to the average seismic lithosphere thickness (Priestley & McKenzie, 2013). On post-LGM (10–20 kyr) timescales, the apparent LAB depth shoals to 70 km in the east to 160 km in the north, with an average value of 120 km (Figure 7c). The apparent LAB depth reaches an average steady-state value of 30–50 km at multi-million-year timescales (Figure 7d). At all frequencies, the pattern of lateral variation in apparent LAB depth is similar, with thinner lithosphere predicted in eastern and southern Greenland, and thicker lithosphere in western and northern Greenland (Figure 7).

5. Discussion

5.1. Contribution of Transient Dissipation to Greenland Upper Mantle Deformation

We computed and averaged the normalized complex viscosity (Equation 6; $\overline{\eta}^*(\omega)$) across Greenland from the seismic LAB down to 400 km, which encompasses the depth range over which a GIA model will typically average the upper mantle viscosity. We found that the domain-averaged $\overline{\eta}^*(\omega)$ is equal to 1 at high (elastic) and low (viscous) frequencies (Figure 8a), indicating that, at these end-member timescales, Greenland upper mantle behavior is well represented by the linear Maxwell model without any significant transient effects. However, in the master curve fit model, $\overline{\eta}^*(\omega)$ drops below 1 within an intermediate frequency band corresponding to timescales of 10^0–10^4 years (Figure 8a). The minimum predicted value of $\overline{\eta}^*(\omega)$ is ~0.44, which occurs at timescales of 10^2–10^3 years (Figure 8a) and is a consequence of additional dissipation from transient elements. The interpretation is that at these timescales, as much as 56% of the observed dissipation may be due to transient creep mechanisms (relative to the equivalent Maxwell model). The extended Burgers model predicts a similarly sized contribution from transient dissipation, albeit over a wider range of timescales (10^{-1}–10^5 years; Figure 8a).

Our results suggest that transient deformation makes its most significant contribution to the rheological behavior of the Greenland upper mantle at loading frequencies corresponding to centennial timescales. These timescales correspond to changes in ice mass during the last millennium (i.e., during and following the LIA), which supports recent inferences made from analysis of GNSS data (Adhikari et al., 2021). We also find that as the timescale of loading increases to multi-millennial timescales, the contribution of transient deformation progressively decreases. At timescales of 10–20 kyr, $\overline{\eta}^* = 0.8$–0.9 (Figure 8a), which implies that deformation occurring today that was induced by ice mass loss immediately following the LGM will contain a smaller (albeit non-negligible) component of transient dissipation compared to LIA ice mass change-induced deformation. At longer timescales that characterize glacial-interglacial cycles and mantle convection (>10^5 years), the contribution of transient dissipation becomes negligible and $\overline{\eta}^*(\omega)$ returns to unity (Figure 8a), indicating realignment with the Maxwell model at the steady-state viscous limit.

5.2. Previous Inferences of Mantle Viscosity and Lithosphere Thickness in Greenland

In this section, we compare our 4D predictions to estimates of mantle viscosity and lithosphere thickness that have been inferred from observations of deformation (e.g., seismic wave velocities, GNSS measurements, RSL

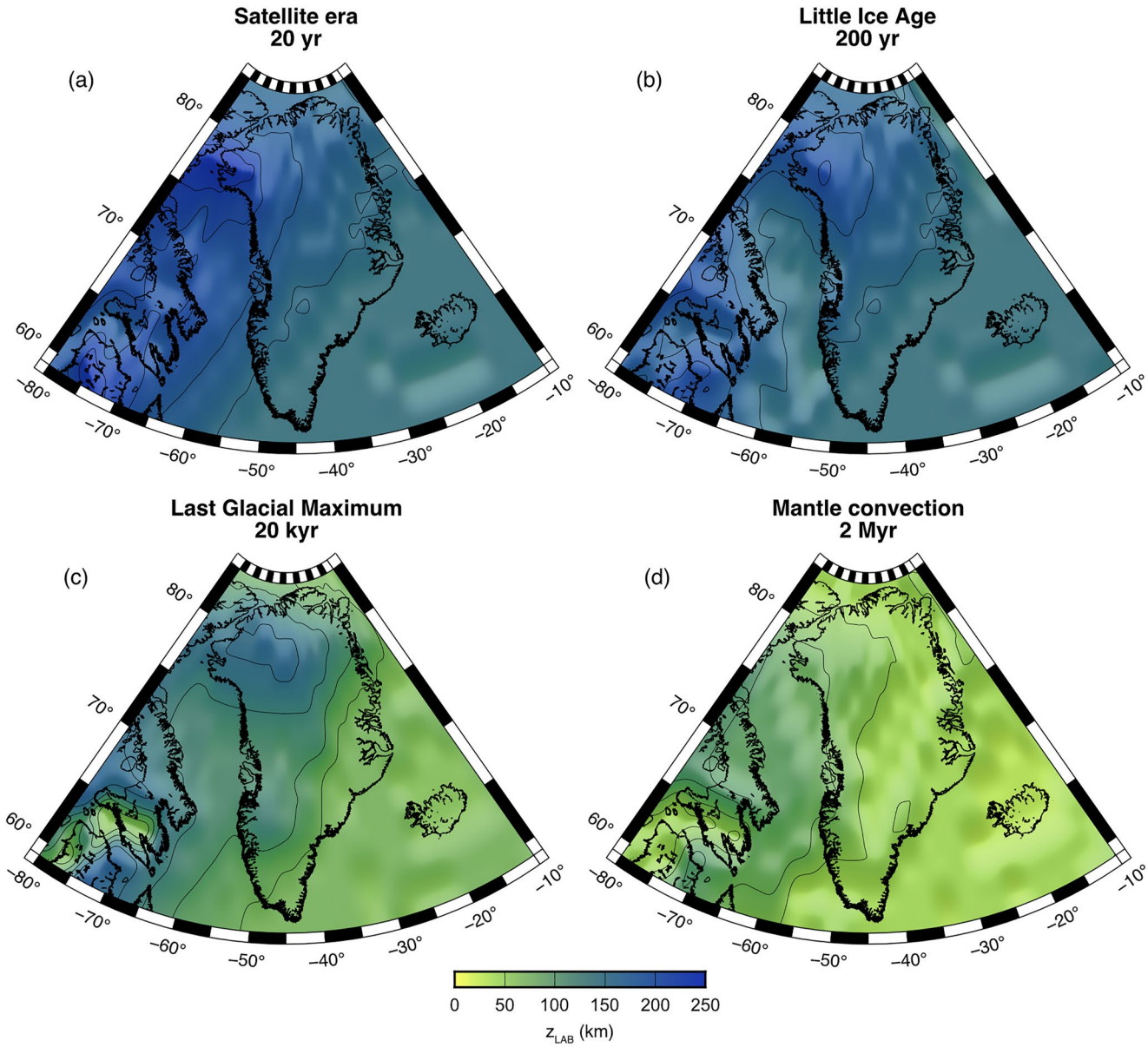

Figure 7. Apparent lithosphere-asthenosphere boundary (LAB) depth (z_{LAB}) for the master curve fit with pre-melting scaling constitutive model. The LAB at any frequency (timescale) is defined as the depth at which the Maxwell frequency is equal to that frequency. Maps show the apparent LAB depth at (a) 20 years, (b) 200 years, (c) 20 kyr, and (d) 2 Myr timescales. Contour interval is 25 km.

data, gravity/geoid anomalies) that pertain to processes operating across a range of timescales (e.g., seismic wave propagation, ice mass change, mantle convection). Although the apparent viscosity computed here is not directly analogous to the viscosity derived by previous studies that fitted a linear Maxwell model to their observational data, we converted these inferred Maxwell steady-state viscosities to the apparent viscosity at the frequency window at which these studies observed mantle deformation using Equation 7 (for more details see Figure S5 and Table S1 in Supporting Information S1).

A key finding from our calculations is that the converted apparent viscosities of 3–6 × 10^{19} Pa s at timescales pertaining to post-LIA ice mass loss (Adhikari et al., 2021) and 5 × 10^{20} Pa s at timescales pertaining to post-LGM ice mass loss (Lecavalier et al., 2014) are in good agreement with the predictions of the master curve fit model at these frequency bands (Figure 8b). At the steady-state limit, where $\|(\eta^*(\omega))\| \rightarrow \eta_0$, our master curve fit calculations predict an average upper mantle η_0 value of ~6 × 10^{20} Pa s in Greenland (Figure 8b), which is also

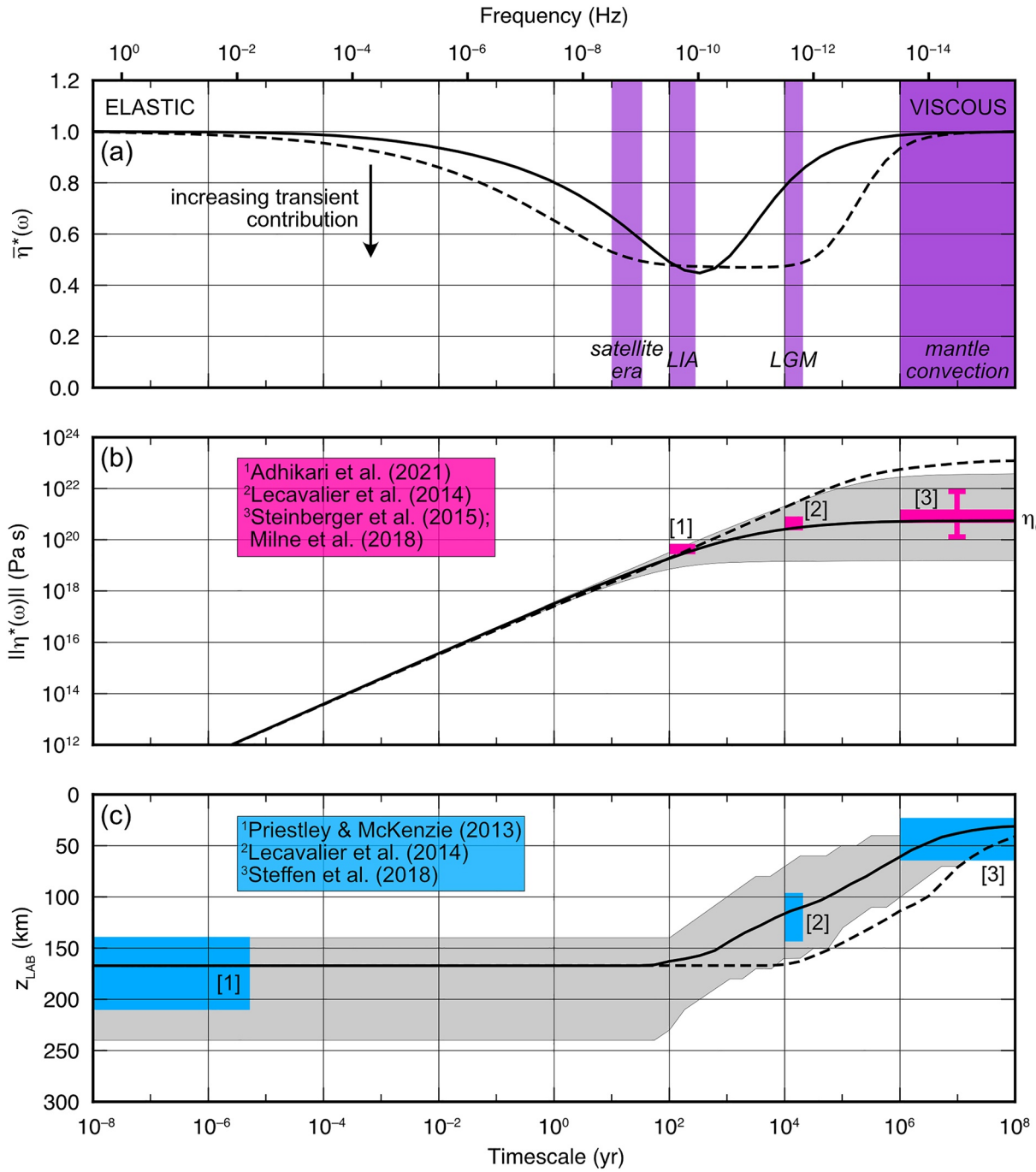

Figure 8. Frequency dependence of apparent mantle viscosity and lithosphere thickness. Calculations using both the master curve fit (solid line) and extended Burgers (dashed line) models are displayed. Black lines represent spatial averages across Greenland and (for viscosity) from z_{LAB} down to 400 km depth; gray shaded regions show the minimum and maximum values within the model domain. (a) Normalized complex viscosity ($\bar{\eta}^*(\omega)$). Deviations of $\bar{\eta}^*(\omega)$ from unity are indicative of a contribution of transient deformation processes. Purple bars illustrate the deformation timescales associated with mantle convection and Little Ice Age (LIA), Last Glacial Maximum (LGM), and satellite era ice mass loss. (b) Apparent viscosity ($\|\eta^*(\omega)\|$). Previous Greenland-wide optimal upper mantle viscosity estimates inferred using the linear Maxwell model (Adhikari et al., 2021; Lecavalier et al., 2014; Steinberger et al., 2015) have been converted to apparent viscosity at the timescale of the observed deformation (magenta boxes). Also shown (vertical bars) is the range in upper mantle steady-state viscosity for a laterally heterogeneous model (Milne et al., 2018). Note that the apparent viscosity reaches a steady-state value (η_0) at the zero-frequency (viscous) limit. (c) Apparent lithosphere-asthenosphere boundary (LAB) depth (z_{LAB}). Previous estimates of optimal/average lithosphere thickness in Greenland (blue boxes) used data sets and methods that pertain to a range of timescales (Lecavalier et al., 2014; Priestley & McKenzie, 2013; Steffen et al., 2018). In panels (b) and (c), the vertical ranges of the colored boxes reflect stated optimal ranges (or standard deviations for spatially heterogenous inferences). If neither is provided, we assumed arbitrary "errors" of ±50% for apparent viscosity and ±25% for z_{LAB} estimates, which are comparable to uncertainties reported in other studies.

in good agreement with the values inferred to match geodynamic observations such as geoid anomalies and heat flux (Steinberger et al., 2015), although the steady-state mantle viscosity is particularly sensitive to the constitutive model used (Figure 8b).

Unfortunately, few estimates of lateral mantle viscosity variations in Greenland currently exist. A recent estimate of the 3D Maxwell viscosity structure (Milne et al., 2018) shows variations in steady-state viscosity at 200 km depth from 10^{20} Pa s in eastern and southern Greenland, 5×10^{20} Pa s through much of central Greenland, and up to 10^{22} Pa s in northern Greenland, which shows broad first-order agreement with our inferred steady-state viscosity patterns (Figure 5d). Moreover, high GNSS uplift rates in eastern Greenland driven by the post-LGM viscous response have been reconciled by an asthenosphere viscosity of 10^{19} Pa s in this region (Khan et al., 2016), which is in agreement with the lowest predicted values in Greenland at these timescales (Figure 8b). However, our computed region of low apparent viscosity in east Greenland is not as spatially confined nor as significant in amplitude as that of Khan et al. (2016).

At high frequencies, the master curve fit and extended Burgers models predict almost identical apparent viscosities (Figure 8b, Figure S4 in Supporting Information S1). By contrast, the extended Burgers model predicts an average upper mantle η_0 value of order 10^{23} Pa s (Figure 8b, Figure S4 in Supporting Information S1). This indicates that master curve fit may be a more appropriate constitutive model than extended Burgers for the Greenland mantle at the zero-frequency limit, with the caveat that the thermodynamic state of the mantle remains uncertain (Figure 6). Despite their different predictions at the zero-frequency limit, which likely relate to intrinsic factors such as different grain size exponents and different scaling relationships (particularly close to the solidus) (Havlin et al., 2021; Ivins et al., 2022), both parameterizations show the same trend in apparent viscosity as a function of frequency, with a consistent increase in apparent viscosity as the timescale of the forcing increases up to the steady-state limit (Figure 8b).

The seismic LAB we derived from the GLAD-M25 tomography model (Lei et al., 2020) shows a spatial pattern consistent with the global lithosphere model of Priestley and McKenzie (2013), which predicts an average seismic lithosphere thickness of 175 ± 35 km in Greenland (Figure 8c, Figure S1 and Table S2 in Supporting Information S1). The depth of the LAB inferred from seismic observations approximates the plate thickness at the infinite frequency limit. Studies that consider Earth deformation at longer timescales (e.g., GIA, flexure; Table S2 in Supporting Information S1) typically infer an apparent plate thickness at the frequency of the particular forcing/loading process under investigation, with the plate considered to be distinct from the underlying mantle in that it behaves elastically (Watts et al., 2013).

Our master curve fit model calculations indicate that the apparent LAB depth in Greenland begins to depart from the seismic LAB depth for forcing occurring at timescales of $>10^2$ years (Figures 7 and 8c). At timescales of 20 kyr, the average apparent LAB depth decreases to 120 km. This is in good agreement with the optimal elastic lithosphere thickness determined using a GIA model to fit post-LGM RSL data (Lecavalier et al., 2014), although this is a relatively weak constraint or potentially a lower limit given the authors did not consider larger possible thicknesses or lateral variability. By contrast, the extended Burgers model predicts that the apparent LAB depth remains close to the average seismic LAB depth of 175 km for timescales up to 10^5 years before shoaling at longer timescales (Figure 8c). The spatial patterns in apparent LAB depth at GIA timescales (Figure 7c) also show agreement with previous model inferences (Conrad & Lithgow-Bertelloni, 2006; Zhong et al., 2003), which show low thicknesses in south and east Greenland and high thicknesses in the north and west. However, our inferred LAB depths show finer-scale variability than these earlier global models. The extended Burgers model shows a similar trend of a reduction in apparent LAB depth as the timescale increases. However, the decrease begins at timescales two orders of magnitude longer than under the master curve fit model (Figure 8c), such that the apparent LAB depth predicted by the extended Burgers model is typically greater than that of the master curve fit.

For the master curve fit model, the average apparent LAB depth shoals to ~30 km at multi-million-year timescales (Figure 8c), although this is capped by the thickness of the crust in the GLAD-M25 tomography model. By comparison, spectral analysis of gravity anomaly data recovered a mean effective elastic thickness (T_e) of the Greenland lithosphere of ~40 km (Steffen et al., 2018). T_e is a parameter commonly used in flexural isostatic modeling, and may be conceptualized as the thickness of a completely elastic plate overlying an inviscid fluid mantle (Watts et al., 2013), which is relevant at the zero-frequency limit for z_{LAB}. The inferred T_e of Greenland exhibits notable lateral heterogeneity, with values as low as 10 km in the south and east and as high as 80 km in the northwest (Figure S1 in Supporting Information S1), whereas our estimated $z_{\mathrm{LAB}}(\omega \to 0)$ is less spatially variable,

with a range of 30–60 km (Figure 7d). This narrow range is likely related to limitations in the vertical resolution of the GLAD-M25 seismic model and uncertainties at shallow depths close to the Moho (Lei et al., 2020). Nonetheless, the general agreement in magnitude between our estimated $z_{\mathrm{LAB}}(\omega \rightarrow 0)$ and T_e estimates derived using different observational data and approaches is encouraging and indicates that the steady-state predictions from the viscous part of the constitutive models are consistent with previous regional-scale geophysical observations.

5.3. Implications for GIA Models

Our findings indicate that, as hypothesized by recent studies (Adhikari et al., 2021; Ivins et al., 2022), transient creep plays an important role in solid Earth deformation over the annual to multi-millennial (10^0–10^4 years) timescales that correspond to significant changes in ice mass, vertical land motion, and RSL in Greenland. Estimates of mantle viscosity that assume a linear Maxwell model with no transient component (Figure 2) may therefore not reflect the steady-state viscosity if they are derived from geodetic or geological data that sample deformation over the timescales where significant transient dissipation occurs. Previous studies have also indicated that loading operating at different spatiotemporal scales may be associated with different viscosities due to (a) stress-dependence (Blank et al., 2021) and (b) sensitivity to the rheology of differing depth intervals in the mantle and changes in the thickness of the elastic lithosphere (Nield et al., 2018). Alongside these mechanisms, we have shown that transient deformation may, in part, explain why studies focusing on post-LIA deformation recover lower viscosity values than those focusing on post-LGM deformation in Greenland (Adhikari et al., 2021).

In addition, these findings have important implications for estimates of mantle viscosity in Antarctica, which also exhibits apparent local spatial and temporal variability (Barletta et al., 2018; Nield et al., 2014; Samrat et al., 2021; Wolstencroft et al., 2015; Zhao et al., 2017) that may, in part, be attributed to transient deformation (Lau et al., 2021) alongside other mechanisms such as depth sensitivity and stress-dependence (Blank et al., 2021; Nield et al., 2018). Further, we caution that taking a mantle viscosity determined from observational data that pertain to changes in RSL over thousands of years and applying this value to models of ice loss and Earth deformation over the past decade may result in the effective viscosity being overestimated (Figure 8b), resulting in uplift rates following (e.g.) rapid deglaciation being significantly underestimated. By contrast, we note that the comparative lack of spatial variation in apparent viscosity predicted at high frequencies (timescales $<10^2$ years; Figure 8b) suggests that the usage of three-dimensional models of mantle viscosity when simulating deformation over decadal timescales may be less of a priority than when modeling deformation over multi-millennial and longer timescales.

Our findings underline the potential importance of incorporating full-spectrum viscoelasticity that captures transient dissipation into GIA models when investigating ice mass and RSL change over recent centuries and millennia. The range of Maxwell viscosities across published studies must be interpreted in the context of possible transient deformation; relating these values to apparent viscosities at the frequency band of deformation offers a pathway to do so. Building a fuller physical understanding of transient deformation, the underlying grain-scale mechanisms that cause it, and how it manifests in the solid Earth's response to changing ice sheets, must remain goals to facilitate improved predictions of future changes in RSL around Greenland in the coming decades. We reiterate that multiple constitutive models for anelastic deformation exist, each relying on empirically derived (and scaled) equations that incorporate parameters that are often poorly constrained, especially in a remote and under-sampled setting such as the Greenland mantle. It is therefore important, given the potential significance of these transient processes, that further work is undertaken to better constrain the thermodynamic state variables (i.e., temperature, grain size, and melt fraction), and the equations that link them to the anelastic properties of the mantle, which would in turn lead to an improved representation of mantle deformation across all timescales.

6. Conclusions

In this study, we have used observations of the seismic properties of the Greenland upper mantle to constrain its thermodynamic state, and in turn self-consistently predict rheological behavior across a broad range of timescales, including the relatively unexplored transient regime. We draw the following conclusions.

1. The apparent viscosity of the Greenland upper mantle increases with the timescale of the forcing/loading being applied. We predict average apparent viscosities of order 10^{19} Pa s for centennial timescales, order

10^{20} Pa s for multi-millennial timescales, and a steady-state value of $\sim 6 \times 10^{20}$ Pa s. This inferred frequency trend is consistent with apparent viscosities derived from previous studies that used a linear Maxwell model to fit observations pertaining to mantle deformation at particular timescales.

2. Transient deformation contributes to the overall dissipation between timescales of 10^0 and 10^4 years, and most significantly (up to 56%) at timescales of 10^2–10^3 years. This may account for the lower-than-expected upper mantle viscosities required to match GNSS uplift rates related to post-LIA (centennial timescale) ice mass loss (Adhikari et al., 2021). This indicates that transient deformation can potentially reconcile seemingly contradictory estimates of Greenland upper mantle viscosity made across the frequency spectrum.
3. We find that the radial and lateral variability in apparent viscosity increases with the timescale of deformation. At decadal-and-shorter timescales, apparent viscosities are notably homogenous, whereas at multi-millennial-and-longer timescales constitutive models predict variations of more than two orders of magnitude, with high viscosities in (e.g.) northern Greenland and low viscosities in (e.g.) eastern regions, as well as a low-viscosity layer in the uppermost mantle (i.e., asthenosphere). This finding implies that the use of 3D models of mantle viscosity is of especial importance when examining lower-frequency deformation.
4. Apparent LAB depths in Greenland also show frequency dependence (as described on a global scale by Watts et al. (2013)), with average values of 170 km inferred for post-LIA timescales, 120 km for post-LGM timescales and 40 km for multi-million-year timescales. These average values are in good agreement with previous estimates derived from GIA and flexure studies, as is the inferred thinner lithosphere in southern and eastern Greenland and thicker lithosphere in the northwest.
5. Although the detailed mineral physics remains uncertain, incorporation of transient rheological models will likely help more fully represent Earth deformation in Greenland (and elsewhere) at timescales from months to thousands of years. This in turn will help facilitate more accurate predictions of past, present, and future patterns of RSL change and coastal evolution around Greenland's inhabited margins.

Conflict of Interest

The authors declare no conflicts of interest relevant to this study.

Data Availability Statement

The GLAD-M25 global adjoint tomography (*Vs*) and QL6 global attenuation (*Q*) models are available via the IRIS Earth Model Collaboration data products webpages: https://doi.org/10.17611/dp/emc.2020.gladm2500.1 and https://doi.org/10.17611/DP/9991844. The Very Broadband Rheology calculator software library is available at https://doi.org/10.5281/zenodo.4317821. The code for the Bayesian inversion used in this study to determine the mantle thermodynamic state from the seismic observations is available at https://doi.org/10.5281/zenodo.6598795.

Acknowledgments

This research was supported by the U.S. National Science Foundation (Navigating the New Arctic; Grant ICER 19-28146) and in part by the Gordon and Betty Moore Foundation through Grant GBMF9123 to the University of Illinois at Urbana-Champaign. The authors acknowledge computing resources from the Columbia University's Shared Research Computing Facility project, which is supported by the NIH Research Facility Improvement Grant 1G20RR030893-01, and associated funds from the New York State Empire State Development, Division of Science Technology and Innovation (NYSTAR) Contract C090171, both awarded 15 April 2010. The authors would like to extend thanks to Andrew Lloyd for providing input on the global adjoint tomography model. The authors would also like to thank Thorsten Becker, Wouter van der Wal, and two anonymous reviewers, whose constructive feedback helped us to improve and clarify several important aspects of the manuscript.

References

Adhikari, S., Milne, G. A., Caron, L., Khan, S. A., Kjeldsen, K. K., Nilsson, J., et al. (2021). Decadal to centennial timescale mantle viscosity inferred from modern crustal uplift rates in Greenland. *Geophysical Research Letters*, *48*(19), e2021GL094040. https://doi.org/10.1029/2021GL094040

Austermann, J., Hoggard, M. J., Latychev, K., Richards, F. D., & Mitrovica, J. X. (2021). The effect of lateral variations in Earth structure on Last Interglacial sea level. *Geophysical Journal International*, *227*(3), 1938–1960. https://doi.org/10.1093/gji/ggab289

Ball, P. W., White, N. J., Masoud, A., Nixon, S., Hoggard, M. J., Maclennan, J., et al. (2019). Quantifying asthenospheric and lithospheric controls on mafic magmatism across north Africa. *Geochemistry, Geophysics, Geosystems*, *20*(7), 3520–3555. https://doi.org/10.1029/2019GC008303

Bao, X., Dalton, C. A., & Ritsema, J. (2016). Effects of elastic focusing on global models of Rayleigh wave attenuation. *Geophysical Journal International*, *207*(2), 1062–1079. https://doi.org/10.1093/gji/ggw322

Barletta, V. R., Bevis, M., Smith, B. E., Wilson, T., Brown, A., Bordoni, A., et al. (2018). Observed rapid bedrock uplift in Amundsen Sea Embayment promotes ice-sheet stability. *Science*, *360*(6395), 1335–1339. https://doi.org/10.1126/science.aao1447

Barnhoorn, A., Van Der Wal, W., Vermeersen, B. L. A., & Drury, M. R. (2011). Lateral, radial, and temporal variations in upper mantle viscosity and rheology under Scandinavia. *Geochemistry, Geophysics, Geosystems*, *12*(1), Q01007. https://doi.org/10.1029/2010GC003290

Bell, D. R., & Rossman, G. R. (1992). Water in Earth's mantle: The role of nominally anhydrous minerals. *Science*, *255*(5050), 1391–1397. https://doi.org/10.1126/science.255.5050.1391

Bernstein, S., Hanghøj, K., Kelemen, P. B., & Brooks, C. K. (2006). Ultra-depleted, shallow cratonic mantle beneath West Greenland: Dunitic xenoliths from Ubekendt Ejland. *Contributions to Mineralogy and Petrology*, *152*(3), 335–347. https://doi.org/10.1007/s00410-006-0109-0

Bernstein, S., Kelemen, P. B., & Brooks, C. K. (1998). Depleted spinel harzburgite xenoliths in Tertiary dykes from East Greenland: Restites from high degree melting. *Earth and Planetary Science Letters*, *154*(1–4), 221–235. https://doi.org/10.1016/s0012-821x(97)00175-1

Bills, B. G., Adams, K. D., & Wesnousky, S. G. (2007). Viscosity structure of the crust and upper mantle in western Nevada from isostatic rebound patterns of the late Pleistocene Lake Lahontan high shoreline. *Journal of Geophysical Research*, *112*(6), 1–18. https://doi.org/10.1029/2005JB003941

Blank, B., Barletta, V., Hu, H., Pappa, F., & van der Wal, W. (2021). Effect of lateral and stress-dependent viscosity variations on GIA induced uplift rates in the Amundsen Sea Embayment. *Geochemistry, Geophysics, Geosystems*, *22*(9), 1–28. https://doi.org/10.1029/2021GC009807

Cammarano, F., Goes, S., Vacher, P., & Giardini, D. (2003). Inferring upper-mantle temperatures from seismic velocities. *Physics of the Earth and Planetary Interiors*, *138*(3–4), 197–222. https://doi.org/10.1016/S0031-9201(03)00156-0

Caron, L., Métivier, L., Greff-Lefftz, M., Fleitout, L., & Rouby, H. (2017). Inverting Glacial Isostatic Adjustment signal using Bayesian framework and two linearly relaxing rheologies. *Geophysical Journal International*, *209*(2), 1126–1147. https://doi.org/10.1093/gji/ggx083

Celli, N. L., Lebedev, S., Schaeffer, A. J., & Gaina, C. (2021). The tilted Iceland Plume and its effect on the North Atlantic evolution and magmatism. *Earth and Planetary Science Letters*, *569*, 117048. https://doi.org/10.1016/j.epsl.2021.117048

Conrad, C. P., & Lithgow-Bertelloni, C. (2006). Influence of continental roots and asthenosphere on plate-mantle coupling. *Geophysical Research Letters*, *33*(5), 2–5. https://doi.org/10.1029/2005GL025621

Dietrich, R., Rülke, A., & Scheinert, M. (2005). Present-day vertical crustal deformations in West Greenland from repeated GPS observations. *Geophysical Journal International*, *163*(3), 865–874. https://doi.org/10.1111/j.1365-246X.2005.02766.x

Durek, J. J., & Ekström, G. (1996). A radial model of anelasticity consistent with long-period surface-wave attenuation. *Bulletin of the Seismological Society of America*, *86*, 144–158. https://doi.org/10.1785/BSSA08601A0144

Dziewonski, A. M., & Anderson, D. L. (1981). Preliminary reference Earth model. *Physics of the Earth and Planetary Interiors*, *25*(4), 297–356. https://doi.org/10.1016/0031-9201(81)90046-7

Eaton, D. W., Darbyshire, F., Evans, R. L., Grütter, H., Jones, A. G., & Yuan, X. (2009). The elusive lithosphere-asthenosphere boundary (LAB) beneath cratons. *Lithos*, *109*(1–2), 1–22. https://doi.org/10.1016/j.lithos.2008.05.009

Evans, R. L., Tarits, P., Chave, A. D., White, A., Heinson, G., Filloux, J. H., et al. (1999). Asymmetric electrical structure in the mantle beneath the East Pacific rise at 17°S. *Science*, *286*(5440), 752–756. https://doi.org/10.1126/science.286.5440.752

Faul, U., & Jackson, I. (2005). The seismological signature of temperature and grain size variations in the upper mantle. *Earth and Planetary Science Letters*, *234*(1–2), 119–134. https://doi.org/10.1016/j.epsl.2005.02.008

Fischer, K. M., Ford, H. A., Abt, D. L., & Rychert, C. A. (2010). The lithosphere-asthenosphere boundary. *Annual Review of Earth and Planetary Sciences*, *38*(1), 551–575. https://doi.org/10.1146/annurev-earth-040809-152438

Forsyth, D. W., Scheirer, D. S., Webb, S. C., Dorman, L. M., Orcutt, J. A., Harding, A. J., et al. (1998). Imaging the deep seismic structure beneath a mid-ocean ridge: The MELT experiment: The MELT seismic team. *Science*, *280*(5367), 1215–1218. https://doi.org/10.1126/science.280.5367.1215

Gribb, T. T., & Cooper, R. F. (1998). Low-frequency shear attenuation in polycrystalline olivine: Grain boundary diffusion and the physical significance of the Andrade model for viscoelastic rheology. *Journal of Geophysical Research*, *103*(B11), 27267–27279. https://doi.org/10.1029/98JB02786

Grose, C. J., & Afonso, J. C. (2013). Comprehensive plate models for the thermal evolution of oceanic lithosphere. *Geochemistry, Geophysics, Geosystems*, *14*(9), 3751–3778. https://doi.org/10.1002/ggge.20232

Hansen, L. N., Zimmerman, M. E., & Kohlstedt, D. L. (2011). Grain boundary sliding in San Carlos olivine: Flow law parameters and crystallographic-preferred orientation. *Journal of Geophysical Research*, *116*(8), 1–16. https://doi.org/10.1029/2011JB008220

Havlin, C., Holtzman, B. K., & Hopper, E. (2021). Inference of thermodynamic state in the asthenosphere from anelastic properties, with applications to North American upper mantle. *Physics of the Earth and Planetary Interiors*, *314*, 106639. https://doi.org/10.1016/j.pepi.2020.106639

Hirth, G., & Kohlstedt, D. L. (2003). Rheology of the upper mantle and the mantle wedge: A view from the experimentalists. *Geophysical Monograph Series*, *138*, 83–106. Retrieved from http://earth.usc.edu/downloads/jplatt/geol535/hirth_kohlstedt_2003.pdf%5Cnpapers3://publication/uuid/08CBD826-A9E7-469F-9EF5-9146ED9CEBB9

Ivins, E. R., Caron, L., Adhikari, S., & Larour, E. (2022). Notes on a compressible extended Burgers model of rheology. *Geophysical Journal International*, *228*(3), 1975–1991. https://doi.org/10.1093/gji/ggab452

Ivins, E. R., Caron, L., Adhikari, S., Larour, E., & Scheinert, M. (2020). A linear viscoelasticity for decadal to centennial time scale mantle deformation. *Reports on Progress in Physics*, *83*(10), 106801. https://doi.org/10.1088/1361-6633/aba346

Jackson, I., & Faul, U. H. (2010). Grainsize-sensitive viscoelastic relaxation in olivine: Towards a robust laboratory-based model for seismological application. *Physics of the Earth and Planetary Interiors*, *183*(1–2), 151–163. https://doi.org/10.1016/j.pepi.2010.09.005

Jaupart, C., & Mareschal, J. C. (2007). Heat flow and thermal structure of the lithosphere. In A. B. Watts & G. Schubert (Eds.), *Treatise on geophysics volume 6. Crust and lithosphere dynamics* (pp. 217–252). Elsevier.

Kang, K., Zhong, S., Geruo, A., & Mao, W. (2022). The effects of non-Newtonian rheology in the upper mantle on relative sea level change and geodetic observables induced by glacial isostatic adjustment process. *Geophysical Journal International*, *228*(3), 1887–1906. https://doi.org/10.1093/gji/ggab428

Karato, S., & Karki, B. B. (2001). Origin of lateral variation of seismic wave velocities and density in the deep mantle. *Journal of Geophysical Research*, *106*(B10), 21771–21783. https://doi.org/10.1029/2001JB000214

Khan, S. A., Sasgen, I., Bevis, M., Van Dam, T., Bamber, J. L., Willis, M., et al. (2016). Geodetic measurements reveal similarities between post–Last Glacial Maximum and present-day mass loss from the Greenland ice sheet. *Science Advances*, *2*(9), e1600931. https://doi.org/10.1126/sciadv.1600931

Khan, S. A., Wahr, J., Leuliette, E., van Dam, T., Larson, K. M., & Francis, O. (2008). Geodetic measurements of postglacial adjustments in Greenland. *Journal of Geophysical Research*, *113*(2), 1–16. https://doi.org/10.1029/2007JB004956

Kjeldsen, K. K., Korsgaard, N. J., Bjørk, A. A., Khan, S. A., Box, J. E., Funder, S., et al. (2015). Spatial and temporal distribution of mass loss from the Greenland Ice Sheet since AD 1900. *Nature*, *528*(7582), 396–400. https://doi.org/10.1038/nature16183

Lau, H. C. P., Austermann, J., Holtzman, B. K., Havlin, C., Lloyd, A. J., Book, C., & Hopper, E. (2021). Frequency dependent mantle viscoelasticity via the complex viscosity: Cases from Antarctica. *Journal of Geophysical Research: Solid Earth*, *126*(11), 1–36. https://doi.org/10.1029/2021JB022622

Lau, H. C. P., & Holtzman, B. K. (2019). "Measures of dissipation in viscoelastic media" extended: Toward continuous characterization across very broad geophysical time scales. *Geophysical Research Letters*, *46*(16), 9544–9553. https://doi.org/10.1029/2019GL083529

Lau, H. C. P., Holtzman, B. K., & Havlin, C. (2020). Toward a self-consistent characterization of lithospheric plates using full-spectrum viscoelasticity. *AGU Advances*, *1*(4), 1–17. https://doi.org/10.1029/2020av000205

Lau, H. C. P., Mitrovica, J. X., Austermann, J., Crawford, O., Al-Attar, D., & Latychev, K. (2016). Inferences of mantle viscosity based on ice age data sets: Radial structure. *Journal of Geophysical Research: Solid Earth*, *121*(10), 6991–7012. https://doi.org/10.1002/2016JB013043

Lecavalier, B. S., Milne, G. A., Simpson, M. J. R., Wake, L., Huybrechts, P., Tarasov, L., et al. (2014). A model of Greenland ice sheet deglaciation constrained by observations of relative sea level and ice extent. *Quaternary Science Reviews*, *102*, 54–84. https://doi.org/10.1016/j.quascirev.2014.07.018

Lei, W., Ruan, Y., Bozdağ, E., Peter, D., Lefebvre, M., Komatitsch, D., et al. (2020). Global adjoint tomography – Model GLAD-M25. *Geophysical Journal International*, *223*(1), 1–21. https://doi.org/10.1093/gji/ggaa253

Long, A. J., Woodroffe, S. A., Roberts, D. H., & Dawson, S. (2011). Isolation basins, sea-level changes and the Holocene history of the Greenland Ice Sheet. *Quaternary Science Reviews*, *30*(27–28), 3748–3768. https://doi.org/10.1016/j.quascirev.2011.10.013

Lyck, L., & Taagholt, J. (1987). Greenland – Its economy and resources. *Arctic*, *40*(1), 50–59. https://doi.org/10.14430/arctic1746

Mankoff, K., Fettweis, X., Langen, P., Stendel, M., Kjeldsen, K., Karlsson, N., et al. (2021). Greenland ice sheet mass balance from 1840 through next week. *Earth System Science Data*, 1–37. https://doi.org/10.5194/essd-2021-131

McCarthy, C., & Takei, Y. (2011). Anelasticity and viscosity of partially molten rock analogue: Toward seismic detection of small quantities of melt. *Geophysical Research Letters*, *38*(18), 3–7. https://doi.org/10.1029/2011GL048776

McKenzie, D. (2000). Constraints on melt generation and transport from U-series activity ratios. *Chemical Geology*, *162*(2), 81–94. https://doi.org/10.1016/S0009-2541(99)00126-6

Milne, G. A., Latychev, K., Schaeffer, A., Crowley, J. W., Lecavalier, B. S., & Audette, A. (2018). The influence of lateral Earth structure on glacial isostatic adjustment in Greenland. *Geophysical Journal International*, *214*(2), 1252–1266. https://doi.org/10.1093/GJI/GGY189

Morlighem, M., Williams, C. N., Rignot, E., An, L., Arndt, J. E., Bamber, J. L., et al. (2017). BedMachine v3: Complete bed topography and ocean bathymetry mapping of Greenland from multibeam Echo sounding combined with mass conservation. *Geophysical Research Letters*, *44*(21), 11051–11061. https://doi.org/10.1002/2017GL074954

Naif, S., Key, K., Constable, S., & Evans, R. L. (2013). Melt-rich channel observed at the lithosphere-asthenosphere boundary. *Nature*, *495*(7441), 356–359. https://doi.org/10.1038/nature11939

Nicholls, R. J., & Cazenave, A. (2010). Sea-level rise and its impact on coastal zones. *Science*, *328*(5985), 1517–1520. https://doi.org/10.1126/science.1185782

Nield, G. A., Barletta, V. R., Bordoni, A., King, M. A., Whitehouse, P. L., Clarke, P. J., et al. (2014). Rapid bedrock uplift in the Antarctic Peninsula explained by viscoelastic response to recent ice unloading. *Earth and Planetary Science Letters*, *397*, 32–41. https://doi.org/10.1016/j.epsl.2014.04.019

Nield, G. A., Whitehouse, P. L., van der Wal, W., Blank, B., O'Donnell, J. P., & Stuart, G. W. (2018). The impact of lateral variations in lithospheric thickness on glacial isostatic adjustment in West Antarctica. *Geophysical Journal International*, *214*(2), 811–824. https://doi.org/10.1093/gji/ggy158

Peltier, W. R., Argus, D. F., & Drummond, R. (2015). Space geodesy constrains ice age terminal deglaciation: The global ICE-6G_C (VM5a) model. *Journal of Geophysical Research: Solid Earth*, *120*(1), 450–487. https://doi.org/10.1002/2014JB011176

Pollitz, F. F. (2003). Transient rheology of the uppermost mantle beneath the Mojave Desert, California. *Earth and Planetary Science Letters*, *215*(1–2), 89–104. https://doi.org/10.1016/S0012-821X(03)00432-1

Priestley, K., & McKenzie, D. (2013). The relationship between shear wave velocity, temperature, attenuation and viscosity in the shallow part of the mantle. *Earth and Planetary Science Letters*, *381*, 78–91. https://doi.org/10.1016/j.epsl.2013.08.022

Rawlinson, N., Fichtner, A., Sambridge, M., & Young, M. K. (2014). Seismic tomography and the assessment of uncertainty. In *Advances in geophysics* (Vol. 55). Elsevier. https://doi.org/10.1016/bs.agph.2014.08.001

Richards, F. D., Hoggard, M. J., White, N., & Ghelichkhan, S. (2020). Quantifying the relationship between short-wavelength dynamic topography and thermomechanical structure of the upper mantle using calibrated parameterization of anelasticity. *Journal of Geophysical Research: Solid Earth*, *125*(9), e2019JB019062. https://doi.org/10.1029/2019JB019062

Samrat, N. H., King, M. A., Watson, C., Hay, A., Barletta, V., & Bordoni, A. (2021). Upper mantle viscosity underneath northern Marguerite Bay, Antarctic Peninsula constrained by bedrock uplift and ice mass variability. *Geophysical Research Letters*, *48*(24), e2021GL097065. https://doi.org/10.1029/2021gl097065

Simon, K. M., Riva, R. E. M., & Broerse, T. (2022). Identifying geographical patterns of transient deformation in the geological sea level record. *Journal of Geophysical Research: Solid Earth*, *127*(7), 1–17. https://doi.org/10.1029/2021JB023693

Simpson, M. J. R., Milne, G. A., Huybrechts, P., & Long, A. J. (2009). Calibrating a glaciological model of the Greenland ice sheet from the Last Glacial Maximum to present-day using field observations of relative sea level and ice extent. *Quaternary Science Reviews*, *28*(17–18), 1631–1657. https://doi.org/10.1016/j.quascirev.2009.03.004

Simpson, M. J. R., Wake, L., Milne, G. A., & Huybrechts, P. (2011). The influence of decadal- to millennial-scale ice mass changes on present-day vertical land motion in Greenland: Implications for the interpretation of GPS observations. *Journal of Geophysical Research*, *116*(2), 1–19. https://doi.org/10.1029/2010JB007776

Sleep, N. H. (2005). Evolution of the continental lithosphere. *Annual Review of Earth and Planetary Sciences*, *33*(1999), 369–393. https://doi.org/10.1146/annurev.earth.33.092203.122643

Spada, G., Ruggieri, G., Sørensen, L. S., Nielsen, K., Melini, D., & Colleoni, F. (2012). Greenland uplift and regional sea level changes from ICESat observations and GIA modelling. *Geophysical Journal International*, *189*(3), 1457–1474. https://doi.org/10.1111/j.1365-246X.2012.05443.x

Steffen, R., Audet, P., & Lund, B. (2018). Weakened lithosphere beneath Greenland inferred from effective elastic thickness: A hot spot effect? *Geophysical Research Letters*, *45*(10), 4733–4742. https://doi.org/10.1029/2017GL076885

Steinberger, B., Spakman, W., Japsen, P., & Torsvik, T. H. (2015). The key role of global solid-Earth processes in preconditioning Greenland's glaciation since the Pliocene. *Terra Nova*, *27*(1), 1–8. https://doi.org/10.1111/ter.12133

Stixrude, L., & Lithgow-Bertelloni, C. (2005). Mineralogy and elasticity of the oceanic upper mantle: Origin of the low-velocity zone. *Journal of Geophysical Research*, *110*(3), 1–16. https://doi.org/10.1029/2004JB002965

Sundberg, M., & Cooper, R. F. (2010). A composite viscoelastic model for incorporating grain boundary sliding and transient diffusion creep; correlating creep and attenuation responses for materials with a fine grain size. *Philosophical Magazine*, *90*(20), 2817–2840. https://doi.org/10.1080/14786431003746656

Takei, Y. (2017). Effects of partial melting on seismic velocity and attenuation: A new insight from experiments. *Annual Review of Earth and Planetary Sciences*, *45*(1), 447–470. https://doi.org/10.1146/annurev-earth-063016-015820

Tarantola, A., & Valette, B. (1982). Generalized nonlinear inverse problems solved using the least squares criterion. *Reviews of Geophysics*, *20*(2), 219–232. https://doi.org/10.1029/RG020i002p00219

van der Wal, W., Whitehouse, P. L., & Schrama, E. J. O. (2015). Effect of GIA models with 3D composite mantle viscosity on GRACE mass balance estimates for Antarctica. *Earth and Planetary Science Letters*, *414*, 134–143. https://doi.org/10.1016/j.epsl.2015.01.001

Watts, A. B., Zhong, S. J., & Hunter, J. (2013). The behavior of the lithosphere on seismic to geologic timescales. *Annual Review of Earth and Planetary Sciences*, *41*(1), 443–468. https://doi.org/10.1146/annurev-earth-042711-105457

Whitehouse, P. L., Gomez, N., King, M. A., & Wiens, D. A. (2019). Solid Earth change and the evolution of the Antarctic Ice Sheet. *Nature Communications*, *10*(1), 503. https://doi.org/10.1038/s41467-018-08068-y

Wolstencroft, M., King, M. A., Whitehouse, P. L., Bentley, M. J., Nield, G. A., King, E. C., et al. (2015). Uplift rates from a new high-density GPS network in Palmer Land indicate significant late Holocene ice loss in the southwestern Weddell Sea. *Geophysical Journal International*, *203*(1), 737–754. https://doi.org/10.1093/gji/ggv327

Yamauchi, H., & Takei, Y. (2016). Polycrystal anelasticity at near-solidus temperatures. *Journal of Geophysical Research: Solid Earth*, *121*(11), 7790–7820. https://doi.org/10.1002/2016JB013316

Zhao, C., King, M. A., Watson, C. S., Barletta, V. R., Bordoni, A., Dell, M., & Whitehouse, P. L. (2017). Rapid ice unloading in the Fleming Glacier region, southern Antarctic Peninsula, and its effect on bedrock uplift rates. *Earth and Planetary Science Letters*, *473*, 164–176. https://doi.org/10.1016/j.epsl.2017.06.002

Zhong, S., Paulson, A., & Wahr, J. (2003). Three-dimensional finite-element modelling of Earth's viscoelastic deformation: Effects of lateral variations in lithospheric thickness. *Geophysical Journal International*, *155*(2), 679–695. https://doi.org/10.1046/j.1365-246X.2003.02084.x

Zwally, H. J., Giovinetto, M. B., Beckley, M. A., & Saba, J. L. (2012). *Antarctic and Greenland drainage systems*. GSFC Cryospheric Sciences Laboratory. Retrieved from http://icesat4.gsfc.nasa.gov/cryo_data/ant_grn_drainage_systems.php